Retrieving Sea Ice Drag Coefficients and Turning Angles From In Situ and Satellite Observations Using an Inverse Modeling Framework

H. D. B. S. Heorton[1] [ID], M. Tsamados[1] [ID], S. T. Cole[2] [ID], A. M. G. Ferreira[1,3], A. Berbellini[1] [ID], M. Fox[1] [ID], and T. W. K. Armitage[4] [ID]

[1]Department of Earth Sciences, University College London, London, UK, [2]Woods Hole Oceanographic Institution, Woods Hole, MA, USA, [3]CERIS, Instituto Superior Técnico, Universidade de Lisboa, Lisboa, Portugal, [4]Jet Propulsion Laboratory, California Institute of Technology, Pasadena, CA, USA

Abstract For ice concentrations less than 85%, internal ice stresses in the sea ice pack are small and sea ice is said to be in free drift. The sea ice drift is then the result of a balance between Coriolis acceleration and stresses from the ocean and atmosphere. We investigate sea ice drift using data from individual drifting buoys as well as Arctic-wide gridded fields of wind, sea ice, and ocean velocity. We perform probabilistic inverse modeling of the momentum balance of free-drifting sea ice, implemented to retrieve the Nansen number, scaled Rossby number, and stress turning angles. Since this problem involves a nonlinear, underconstrained system, we used a Monte Carlo guided search scheme—the Neighborhood Algorithm—to seek optimal parameter values for multiple observation points. We retrieve optimal drag coefficients of $C_A = 1.2 \times 10^{-3}$ and $C_O = 2.4 \times 10^{-3}$ from 10-day averaged Arctic-wide data from July 2014 that agree with the AIDJEX standard, with clear temporal and spatial variations. Inverting daily averaged buoy data give parameters that, while more accurately resolved, suggest that the forward model oversimplifies the physical system at these spatial and temporal scales. Our results show the importance of the correct representation of geostrophic currents. Both atmospheric and oceanic drag coefficients are found to decrease with shorter temporal averaging period, informing the selection of drag coefficient for short timescale climate models.

1. Introduction

Sea ice floats upon the polar oceans where it is at the mercy of winds and ocean currents. The resulting drift of sea ice plays a role in the basin-wide thickness distribution (Hibler, 1979), total sea ice volume and ocean circulation (Aagaard & Carmack, 1989; Rudels, 2011), and regional (Haine et al., 2015; Holland et al., 2006) and global climate feedbacks (Petrie et al., 2015). In warmer climates, winds blowing across the open ocean give rise to currents and ocean circulation patterns (Rio & Hernandez, 2003). In the polar oceans, the presence of sea ice complicates this mechanism, acting as an insulating layer between the atmosphere and ocean and modulating the transfer of momentum from the atmosphere to the ocean (Martin et al., 2014).

The momentum transfer between the atmosphere and ocean gives rise to Arctic Ocean circulation patterns including the Beaufort Gyre in the western Arctic Ocean. Recent changes in sea ice extent and thickness have had an effect on its surface roughness characteristics and thus the momentum transfer through it (Martin et al., 2016). This change, along with changing atmospheric conditions, has resulted in the strengthening of the Beaufort Gyre with an increased gradient in dynamic ocean topography (Giles et al., 2012). These changes in the ocean circulation have influenced the extent of Arctic sea ice by the transport of ocean heat to the overlying ice cover (Carmack et al., 2015; Davis et al., 2016; Rippeth et al., 2015).

The vertical momentum flux can be described by atmospheric, τ_A, and oceanic, τ_O, stress terms applied to the sea ice cover. The stress terms represent the turbulent momentum flux (described in section 2.1) or the mean vertical variation in flow speed from a measurement height to the ice interface and are often given in quadratic form (Leppäranta, 2005) with

$$\tau_A = \rho_A C_A e^{i\theta_A} |\mathbf{U}_A| \mathbf{U}_A \qquad (1a)$$

$$\boldsymbol{\tau}_O = \rho_O C_O e^{i\theta_O} |\mathbf{U}_{\mathrm{OI}}| \mathbf{U}_{\mathrm{OI}} \tag{1b}$$

where C_A, C_O, and θ_A, θ_O are the drag coefficients and turning angles for the atmospheric and ocean drag terms respectively, $\mathbf{U}_A$ is the wind velocity, $\mathbf{U}_{\mathrm{OI}}$ is the relative ocean-ice velocity, that is, $\mathbf{U}_{\mathrm{OI}} = \mathbf{U}_O - \mathbf{U}_I$, where $\mathbf{U}_O$ and $\mathbf{U}_I$ are the ocean and ice velocity, respectively, and ρ_A and ρ_O are the densities of the atmosphere and ocean. In the remainder of this paper all values of $\mathbf{U}_{\mathrm{OI}}$ are given with superscripts to accurately define the ocean current considered. The magnitude of C_A depends on the roughness characteristics of sea ice, as addressed in this paper, and the turbulent stability of the atmosphere, as discussed below. C_O depends on the sea ice basal roughness. In the stratified ocean, buoyancy effects must be accounted for (McPhee, 2012), and internal waves will interact with the morphology of the under-ice topography (e.g., keels, McPhee & Kantha, 1989).

The turbulent transfer of momentum from the atmosphere to Earth's surface is described by the Monin-Obukhov similarity theory (Monin & Obukhov, 1954). The drag coefficient C_A represents the magnitude of the total transfer and is often given in the form

$$C_A = C_{An} f_m,$$

where C_{An} is the neutral drag coefficient that depends on the state of the sea ice (form drag and skin drag, e.g., Lu et al., 2011) and f_m is a stability-dependent correction function, often given in functional form along with turbulent heat transfer and which depends on surface potential temperature and humidity (Grachev et al., 2007; Lüpkes & Gryanik, 2015). The state of the atmospheric boundary layer in the Arctic can change from weakly unstable to very stable cases (Grachev et al., 2007), represented by changing values of f_m. Martin et al. (2016) presented a modeling study that considers both the sea ice state-dependent neutral atmospheric drag and the stability correction to the total drag. Their calculated total and neutral drag coefficients were similar for the summer months considered in the present study. Lüpkes and Gryanik (2015) presented a parameterization showing that the neutral and total atmospheric drag coefficient can be similar during atmospheric conditions typical of the summer marginal ice zone (MIZ). Due to these results and the complexity of atmospheric stability correction routines (Andreas et al., 2010; Lüpkes & Gryanik, 2015), we focused upon the total atmospheric drag coefficient C_A in this study and leave the inclusion of atmospheric stability within a inverse model for a future study.

The choice of depth for $\mathbf{U}_{\mathrm{OI}}^d$ represents the measurements available when forcing a coupled or stand-alone sea ice climate model (Tsamados et al., 2014) or when analyzing observation data (such as in the studies discussed in section 2 and by Meneghello et al., 2018). This study considered the case of both surface $\mathbf{U}_{\mathrm{OI}}^{d=6m}$ and geostrophic $\mathbf{U}_{\mathrm{OI}}^g$ or geostrophic equivalent $\mathbf{U}_{\mathrm{OI}}^{ge}$ relative currents measured at the bottom of the ocean mixed layer. For the data used in this study and discussed in section 2, the satellite current $\mathbf{U}_O^g$ is derived from the dynamic ocean topography obtained as the difference between sea surface elevation and geoid (Armitage et al., 2016). Direct buoy measurements capture the ocean currents or relative sea ice ocean currents $\mathbf{U}_{\mathrm{OI}}^{ge}$ that arise due to the dynamic ocean topography, as well local and baroclinic components. Our inverse modeling framework assessed the dynamical consistency of both the satellite-based and point measured data sets.

The total momentum flux between the atmosphere, sea ice, and ocean depends on the four parameters within the quadratic stress C_A, C_O, θ_A, and θ_O. Values for these four parameters were presented following the AIDJEX projects 1972–1976 by McPhee (1976) and Coon (1980) where observations of ice drift were related to winds and have been used widely since. Subsequent studies have deduced parameters from observations of boundary layer turbulence and other processes, summarized in Table 2. For the atmospheric drag, C_A, values vary in the range 0.5–5.6×10^{-3}, with variations due to ice type (Overland & Davidson, 1992) and atmospheric boundary layer stratification (Guest et al., 1995) among others. The oceanic drag coefficient C_O, is between 0.4 and 20.0×10^{-3} (Lu et al., 2011) with variation due to sea ice roughness lengths (Shaw et al., 2008) and the ocean mixed layer conditions (McPhee, 2012; McPhee & Kantha, 1989; Randelhoff et al., 2014). The highest values in this range occur for rough floes or broken floes within the MIZ with the majority of observations within the range 1.3–10.0×10^{-3} (Lu et al., 2011; Shaw et al., 2008). The turning angles θ_A and θ_O are less widely studied and θ_A is stated to be $0°$ in all available literature, while θ_O is estimated from the Ekman spiral (Ekman, 1905) within the ocean mixed layer. Due to the formation of the spiral, θ_O is observed to increase with the depth of reference current (hereafter cited as CTLT; Cole et al., 2017) and is given between $4°$ and $35°$ depending on the observational depth. Due to their importance within climate models,

variability of the drag coefficients and turning angles has been studied using numerical sensitivity studies. Lüpkes et al. (2012) and Tsamados et al. (2014) presented and implement variable C_A and C_O that depend on sea ice type, matched to observational values and with 0° turning angles. Castellani et al. (2014) extracted the height and spacing of obstacles (pressure ridges for example) from laser altimetry data to force a parameterization of C_A similar to that of Lüpkes et al., showing variability between different regions of the Arctic Ocean. Petty et al. (2017) used the same parameterization with airborne observations of sea ice conditions to produce Arctic maps and time series of C_A. Elvidge et al. (2016) performed extensive validation for the Lüpkes et al. (2012) parameterization from airborne observations of eddy-covariance-derived neutral atmospheric drag. Renfrew et al. (2019) tested the atmospheric sensitivity of the Lüpkes et al. parameterization in a fully coupled model.

The quadratic drag laws in equation (1) have been used to investigate the detailed structure of the Beaufort Gyre (Meneghello et al., 2018; Yang, 2009; Zhong et al., 2017), wider Arctic (Dewey et al., 2017), and the Ross Gyre in the Antarctic (Dotto et al., 2018). Reanalysis-derived winds (e.g., Dee et al., 2011) along with satellite-derived ice drift and dynamic ocean topography-derived geostrophic currents (e.g., Armitage et al., 2017; Kimura et al., 2013) were combined through the stress laws to estimate the Ekman pumping and upwelling and downwelling rates, distinguishing the dominating factors for each. However, all of these studies used the drag values given by AIDJEX, quoting them as the "community standard," a trend that has led to little questioning of the correct application of the values. There is yet a need for a sensitivity analysis of observation-derived Ekman pumping rates to ocean and atmospheric sea ice drag laws or chosen parameter values. McPhee (2012) provided mathematical reasons that quadratic drag laws with constant parameter spaces oversimplify the wind-ice-ocean dynamical system, particularly during shallow mixed layer depths or times of melt (Randelhoff et al., 2014). Further uptake on these issues has been limited due to the complexities of more sophisticated schemes that rely on knowledge of the local sea ice cover (Lu et al., 2011; Lüpkes et al., 2012), atmospheric stability (Andreas et al., 2010; Lüpkes & Gryanik, 2015), and the state of the mixed layer (McPhee & Kantha, 1989), and furthermore the difficulty of observational validation.

In this paper we present full probabilistic inversions of the momentum balance of free-drifting sea ice. The inversion used the high fidelity data set of CTLT (see section 2.1) that gave us coincident wind, ice, and ocean mixed layer velocity fields on hourly timescales. These data gave us information about both the average motion on daily and longer timescales and also the variance of each datum. These data were inverted using the surface and geostrophic current inverse model $\mathbb{I}_g^d$ described in section 3.3. We built upon the inversions of this dense, high-frequency data to look at reanalysis and satellite data that span the entire Arctic Basin (see section 2.2). We inverted these data using the geostrophic current-only inverse model $\mathbb{I}_g$ described in section 3.4. This study was a proof of concept for the inversion method of multiple vector fields through a nonlinear forward model and introduces a method for analysis of sea ice momentum balances and drag laws. Here we present our estimates of parameters best applicable to observed wind, ice, and ocean conditions based on the probabilistic inversion of high quality data. Moreover, we present a rigorous mathematical appraisal of the forward model used in this study.

2. Data

We required observations of wind, ice drift, and ocean current velocity in conditions for which there is little internal ice stress, which corresponds to 15–85% ice concentration (lower limit in practice for ice detection). Two data sets were used during the same time period for comparison, namely, the buoy data of CTLT and satellite and reanalysis-based records.

2.1. In Situ Observations for Surface and Geostrophic Current Inverse Model $\mathbb{I}_g^d$

The point observations of CTLT, in particular Buoy Arrays 2, 3, and 4 were collected by ITP-Vs (Ice-Tethered Profilers equipped with instrumentation to measure ocean velocity profiles) and adjacent ice-mass balance and wind observations. We utilize wind velocity, relative ice-to-ocean velocity, ice drift velocity, and ice thickness. The wind measurements were recorded on 1- to 3-hr intervals by an autonomous weather station at 2-m height. We used buoy-recorded wind direction and did not rotate the data to be parallel to coincident ERA data as done by CTLT. The ocean velocity was recorded in two modes: (i) surface currents were recorded at approximately 1 Hz for three 20-min periods per day that we averaged for our surface currents and (ii) four depth current profiles were performed each day with the instrument descending to 250-m depth that we used for the geostrophic equivalent current at the ocean mixed layer base. The surface current speed is
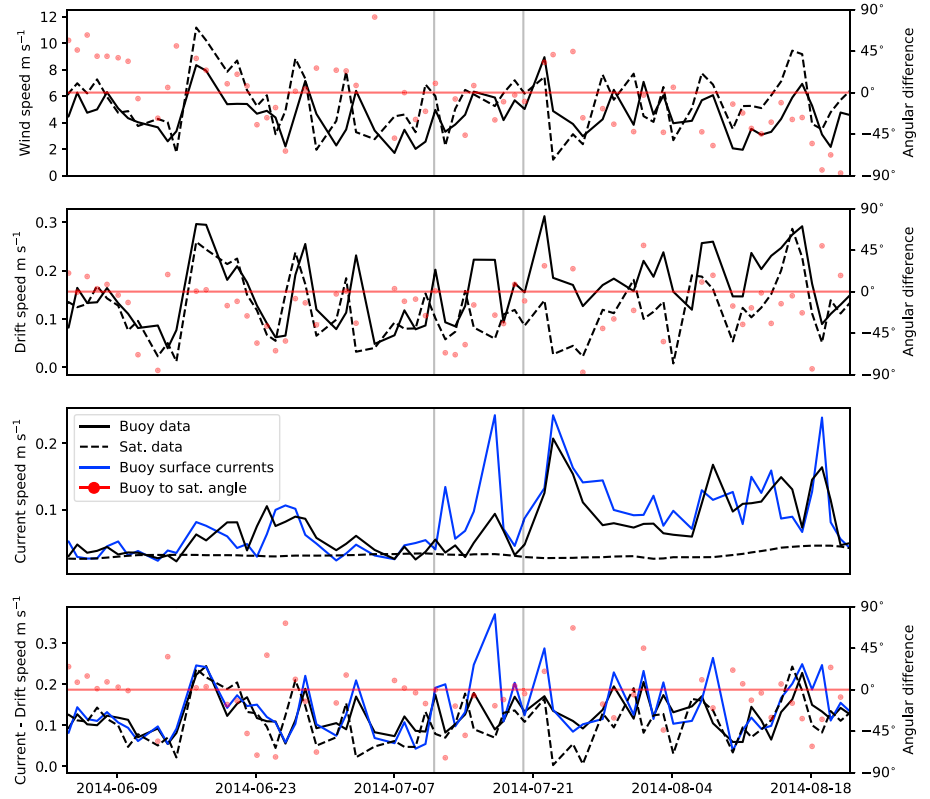
Figure 1. Time series of filtered input data from Buoy Array 2 (solid lines) and coincident satellite/reanalysis data (dashed lines). The angular difference between the two data sources is also plotted (red points). Plotted first is the wind speed (top), second the sea ice drift speed, third the ocean current speed, and fourth the relative ice-to-ocean current speed. The ocean currents compared are the buoy geostrophic equivalent $|\mathbf{U}_O^{ge}|$ and satellite geostrophic currents $|\mathbf{U}_O^{g}|$. Additionally the buoy surface current $|\mathbf{U}_O^{d}|$ is plotted (blue lines). The vertical lines indicate the window of data used for the inversions in Figures 3 and 4. The data were filtered to make it suitable for inversion using the method described in section 4.1. Additional plots for Buoy Arrays 3 and 4 are available in supporting information Figures S1 and S2.

typically greater than the geostrophic equivalent current speed (blue vs. black solid lines in Figure 1). The GPS location of the ice tethered arrays was recorded hourly giving ice drift velocity. Each velocity datum has a time stamp, which allowed us to collect and average the data in any period required for the inverse model analysis. CTLT performed extensive analysis of this data set and have supplied additional data for comparison: turbulence-derived ocean-to-ice stress coefficients, ocean mixed layer depth, and ocean density profiles. These data were chosen as they give high-quality wind, ice, and current flow for lower ice concentrations (available from the National Snow and Ice Data Center SSMI satellite data set; Cavalieri, 1996), which allowed us to consider the momentum balance of ice drift with no contribution from internal stresses within the ice pack. We analyzed the data from 1 June 2014 to the end of each buoy record. The data filtering and averaging methods for each inversion are documented in section 4.1. To invert these data that contain both surface $\mathbf{U}_{OI}^{d}$ and geostrophic equivalent $\mathbf{U}_{OI}^{ge}$ currents, we used inverse model $\mathbb{I}_g^d$ described in section 3.3.

CTLT also presented a time series for C_O that they derived from turbulent momentum flux $< u'w' >, < v'w' >$ where $u', v',$ and w' are the component deviations to the mean flow measured every 4 s and low-pass filtered. The friction velocity

$$u_* = \left(<u'w'>^2 + <v'w'>^2 \right)^{\frac{1}{4}}$$

was then used to give the drag parameter C_d with

$$u_*^2 = C_d (\mathbf{U}_I - \mathbf{U}_O^d)^2$$

with C_d applicable to the depth of ocean current measurement U_O^d, in this case $d = 6$ m.

2.2. Satellite and Reanalysis Data for Geostrophic Current-Only Inverse Model $\mathbb{I}_g$

Satellite and reanalysis data were also available for the Arctic Ocean. We took the ERA-interim reanalysis for 10-m wind speeds (Dee et al., 2011), the ice drift data product of Kimura et al. (2013), and geostrophic currents estimated from satellite-derived dynamic ocean topography given by Armitage et al. (2017, 2016). The wind data field used in this paper is the only data source that comes from a modeling study due to sparsity of weather stations in the Arctic Ocean. The ERA-Interim reanalysis used a surface turbulence parameterization (Dee et al., 2011) that has no analogous value for C_A but will have an effect on the results in this paper. For example, if an alternative reanalysis product was used that has lower Arctic wind speeds, we would expect inversions using this product to give higher values for C_A. For direct comparisons to the buoy data, the satellite data were regridded locally. For each day where buoy data were analyzed, a 100-km-wide local grid with 2-km resolution was constructed centered about the buoy array aligned to its coordinate system. The satellite data were interpolated onto this grid and the vector average and vector standard deviation across it were calculated as inputs data for our developed inverse model. For the Arctic Ocean-wide satellite data inversion a grid of 100-km resolution was used with each interpolated point an input data for the inverse model. As the inversion method for the maps presented used 10-day averages, the variance measure for each datum is taken from the variance over the averaging time period. To invert these data with geostrophic currents $\mathbf{U}_{\mathrm{OI}}^g$ only, we used inverse model $\mathbb{I}_g$ described in section 3.4.

2.3. Data Comparisons

There was a strong correlation between the buoy and reanalysis wind and satellite ice drift data. The daily averaged wind magnitudes have correlation of 0.70 between the buoy and satellite data. The buoy array wind speed was typically 90% of the coincident ERA wind speed (see Figure 1 and supporting information Figures S1 and S2) that we attribute to buoy array records at 2 m, and the reanalysis taken at 10 m. The daily ice drift magnitudes had a correlation of 0.58 between the buoy and satellite data. The ice drift speed from the two data sets had reduced correlation from August onward, which we attribute to melt and the disintegration of ice floes reducing the effectiveness of the satellite image velocity tracking.

The ocean current data from the two sources had fundamental differences and are thus difficult to compare. The satellite geostrophic currents $\mathbf{U}_{\mathrm{OI}}^g$ were estimated from two-dimensional hydrographical data relative to a surface of no-motion. For the buoy data the spatial variation is not available and we took a geostrophic equivalent $\mathbf{U}_{\mathrm{OI}}^{ge}$ at the depth of the mixed layer base given by CTLT. The velocity measurements taken at this depth do appear to avoid the most significant eddies (see CTLT) but are still likely to contain a significant baroclinic component, particularly as the mixed layer laminates and the base becomes less well resolved. Armitage et al. (2016, 2017) performed extensive in situ data comparisons to the dynamic ocean topography and geostrophic currents, and further monthly time period analysis of buoy geostrophic current measurements can be performed as a comparison but are beyond the scope of this study. Detailed spectrum analysis between all the data used in this study will be performed similar to that by Rio and Hernandez (2003) for the open ocean in a future study.

3. The Free Drift Momentum Balance as an Inverse Problem

First, we define the forward model **g** that uses a model **g** to describe the interaction and momentum transfer between the elements of the data vector **d**: winds, sea ice drift, and ocean currents. In this study the model **m** is the set of parameters we sought optimal values for. A large number of models were considered during each inversion (every point in Figures 4 and 7 an evaluated model), and multiple best fitting models were found (every point on the lines of Figures 5 and 8 and pixels of Figure 9). One forward model **g** was considered (equation (3) below) adapted to consider two data formats (equations (5) and (8) below). We describe our approach of seeking optimal models **m** in the subsequent subsections.

3.1. The Free Drift Momentum Balance

As briefly explained in section 1, fragmented sea ice, when collisions between sea ice floes are either rare or transmit negligible inertia, when internal ice stresses cannot be transmitted over distance greater than a floe width, then sea ice is said to be in free drift. The rate of change of momentum is then balanced by wind and ocean stresses τ_A, τ_O, Coriolis and ocean surface tilt forces (see Figure 2) and expressed mathematically as

$$M_I \frac{D\mathbf{U}_I}{Dt} = \boldsymbol{\tau}_A + \boldsymbol{\tau}_O + M_I f_c i(\mathbf{U}_O - \mathbf{U}_I), \tag{2}$$
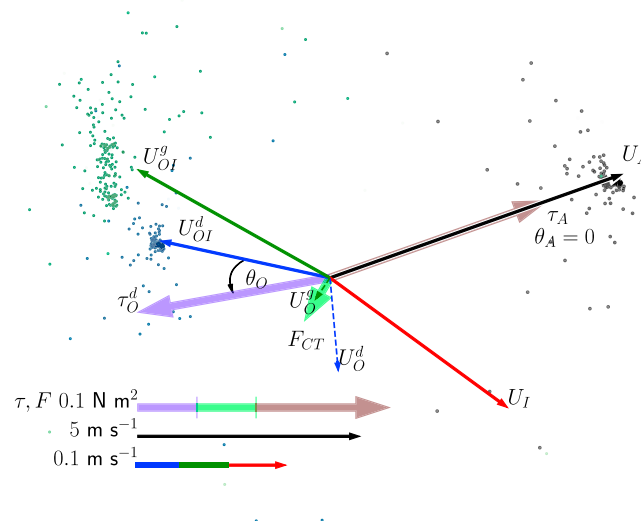
Figure 2. Vectors of free-drifting sea ice that are used in this study's synthetic inversion tests. The idealized data vectors are wind velocity $\mathbf{U}_A$ (black), surface ocean-ice velocity $\mathbf{U}_{OI}^d$ (blue), and geostrophic ocean-ice velocity $\mathbf{U}_{OI}^g$ (green), with associated drag forces τ_A and τ_O and Coriolis/tilt force F_{CT}. Additionally, we show the individual ice velocity $\mathbf{U}_I$ (red) and ocean surface and geostrophic currents (dashed) illustrating an Ekman spiral. The vectors in this figure are calculated using the AIDJEX model values (see Table 1; Coon, 1980; McPhee, 1976). The results from the synthetic inversion test in section 3.6 are represented by points scattered around each observation vector used. The aim of this paper is to appraise the forward model that was used to create this idealized scenario from observations.

(i.e., Heorton et al., 2014) where the left-hand side is the rate of change in momentum, $M_I = \rho_I h_I$ is the unit mass of sea ice with density ρ_I and thickness h_I, f_c is the Coriolis parameter and $i = \sqrt{-1}$, with the vectors expressed in complex notation.

Taking the average sea ice drift over timescales greater than a day, we assumed that the net acceleration of the sea ice is negligible, removing the left-hand side of equation (2). This assumption, along with zero internal ice stresses, is the key assumptions of steady state free-drifting sea ice with their implications discussed in section 5. While several formulations for the drag terms exist (McPhee, 2012), the most widely used are the quadratic drag laws in equation (1). The momentum balance (2) can be expanded in complex notation as

$$\rho_A C_A e^{i\theta_A}|\mathbf{U}_A|\mathbf{U}_A + \rho_O C_O e^{i\theta_O}|\mathbf{U}^d{}_{OI}|(\mathbf{U}^d{}_{OI}) + i\rho_I h f_c(\mathbf{U}^g{}_{OI}) = 0, \tag{3}$$

where C_A, C_O and θ_A, θ_O are the drag coefficients and turning angles for the total atmospheric and ocean drag terms, respectively, $\mathbf{U}_A$ is the wind velocity, and $\mathbf{U}_{OI} = \mathbf{U}_O - \mathbf{U}_I$ is the vector difference or relative ocean-ice velocity at a chosen depth for drag measurements $\mathbf{U}_{OI}^d$ (6- to 7-m fixed depth records for the results in section 4.1) or for the geostrophic current $\mathbf{U}_{OI}^g$.

3.2. The Observation and Model Spaces

The forward model in equation (3) gave us two equations in the x, y or real and imaginary planes but has four distinct physical parameters. The inverse problem is thus underconstrained, and multiple combinations of model parameter values will give similar fits to the data. When using a single data point/vector at a given time j $\mathbf{d}_j$, trade-offs are expected as there will be multiple parameter combinations that can predict very similar data. For example, in a simple linear regression problem $y = mx + c$ and a given single data point x, y, the slope, m, and intercept, c, will trade-off against each other such that similar y will be predicted at a given x value for a set of m, c pairs. More information about this toy problem can be obtained by using additional x, y data. A similar approach can be taken for our forward model expressed by equation (3). Additional constraints can be incorporated into the inversion by using a constant parameter space over many momentum balances, each with their own datum. This method essentially assumes that the model $\mathbf{m}$ is constant for a region of ice cover and will change on timescales greater than the range of data used. This is consistent with the timescale of sea ice melt (10–50 days) against the local variation in wind strength (1–2 days).

The physical system represented by the chosen data is the momentum exchange between wind, ice, and ocean. This system is dominated by the ratio of wind $\mathbf{U}_A$ to relative sea ice-to-ocean velocity $\mathbf{U}_{OI}$, with

the general solution expressing $\mathbf{U}_{OI}$ as a function of wind forcing given in Appendix A. Leppäranta (2005) showed that in the limiting case of thin ice ($h_I \to 0$) or high wind velocity ($\mathbf{U}_A \to 10$ m/s) the ratio of the magnitude of these vectors is equal to the Nansen number, $Na = \sqrt{(\rho_A C_A)/(\rho_O C_O)}$, while their relative orientation $\theta \to \theta_{OA} = \theta_O - \theta_A$ (see Figure 2). Leppäranta (2005) presented the Nansen number describing the wind speed factor of ice drift and introduced the Rossby number $Ro = (\rho_I h_I f_c)/(\rho_O C_O Na|\mathbf{U}_A|)$ describing the Coriolis acceleration factor to complete the scaling of the momentum balance (both described fully in section 3.2). Leppäranta (2005) gave the Nansen number as 2.5% and 3.5% for Arctic and Antarctic surface winds, with the variation attributed to the ratio of atmospheric and oceanic sea ice stress at each location. For the case of thin sea ice, Coriolis acceleration will have a lesser influence and the Rossby number tends to vanish. For sea ice greater than 2 m thick, with a high ice-to-ocean surface stress the Rossby number increases toward 2. Thorndike and Colony (1982) fitted observations to the momentum sea ice equations (2) and analyzed special case solutions of (i) no wind, (ii) low wind, and (iii) high wind. These limiting cases show that to first order Na^2 and θ_{OA} are the only two quantities obtainable during high wind speeds, during which wind and ocean drags dominate the Coriolis and tilt forces ($F_{CT} = M_I f_c i(\mathbf{U}_O - \mathbf{U}_I)$) and also internal sea ice stresses. In order to relate these two quantities back to the parameters of interest, we considered the parameter $Ro' = \rho_I/(\rho_O C_O) = Ro(Na|\mathbf{U}_A|)/(h_I f_c)$, which is the Rossby number in the reduced form that is invariant over the multiple data points chosen. Thus, we have the four-dimensional parameter space of

$$
\mathbf{m} = \begin{pmatrix} Na^2 & = \frac{\rho_A C_A}{\rho_O C_O} \\ Ro' & = \frac{\rho_I}{\rho_O C_O} \\ \theta_{OA} & = \theta_O - \theta_A \\ \theta_A & \end{pmatrix} = \begin{pmatrix} m_1 \\ m_2 \\ m_3 \\ m_4 \end{pmatrix}. \tag{4}
$$

When searching directly for individual drag coefficients and turning angles, our inverse model often produced the trivial result of $C_A, C_O \to 0$. This result has been circumvented by searching for the ratio of C_A, C_O within the Nansen number Na^2. The parameter space in equation (4) allowed us to determine a best fitting value for Na^2 when multiple solution pairs of C_A, C_O were possible, for example, during the high wind speed cases described by Thorndike and Colony (1982).

3.3. Inverting Surface and Geostrophic Currents: Inverse Model $\mathbb{I}_g^d$

We defined the observational set for this inverse problem as a coincident measurement of winds $\mathbf{U}_A^o$ and relative ocean-to-ice velocity at a near-surface depth $\mathbf{U}_{OI}^{d,o}$ and at the equivalent depth of geostrophic motion $\mathbf{U}_{OI}^{ge,o}$. The data vector for time point j is

$$
\mathbf{d}_j = (\mathbf{U}_{A_x}^o, \mathbf{U}_{A_y}^o, \mathbf{U}_{OI_x}^{d,o}, \mathbf{U}_{OI_y}^{d,o}, \mathbf{U}_{OI_x}^{ge,o}, \mathbf{U}_{OI_y}^{ge,o})_j. \tag{5}
$$

Multiple combined data vectors from adjacent time points were considered for each inversion. The j subscript is included to differentiate between each data vector used within the same inversion.

3.3.1. Inverse Model Misfit Functions and Implementation

For the data given, $\mathbf{d}_j$ (equation (5)), and a proposed model $\mathbf{m}$ (equation (4)), we quantified the fit between the forward model and data by a series of misfit functions. The first of the chosen misfit functions is the magnitude of the residual force balance $\mathcal{M}_{FB}$, derived from combining equation (3), parameters $\mathbf{m}$ (equation (4)), and velocity vectors from $\mathbf{d}_j$ and taking its absolute value

$$
\mathcal{M}_{FB_j} = \frac{1}{\sigma_{FB}} \left| \left(\frac{m_1}{m_2} \rho_I \exp(im_4) |\mathbf{U}_{A_j}^o| \mathbf{U}_{A_j}^o \right. \right.
$$
$$
\left. \left. - \frac{\rho_I}{m_2} \exp(i(m_3 + m_4)) |\mathbf{U}_{OI_j}^{d,o}| \mathbf{U}_{OI_j}^{d,o} + i\rho_I h_I f_c \mathbf{U}_{OI_j}^{ge,o} \right) \right|^2, \tag{6}
$$

where σ_{FB} is a representative variation for the force balance that we took as the maximum normalized standard deviation of each component of $\mathbf{d}_j$.

A misfit function was obtainable for each velocity data by comparison to a corresponding model predicted velocity. When using wind, surface, $\mathbf{U}_{OI}^d$, and geostrophic, $\mathbf{U}_{OI}^{ge}$, buoy measured currents, any velocity vector can be calculated from the forward model, evaluated model $\mathbf{m}$ and the other two velocity vectors, see the

appendix, equations (A5)–(A7). We compared observed $\mathbf{U}_A^o$, $\mathbf{U}_{\text{OI}}^{d,o}$, and $\mathbf{U}_{\text{OI}}^{ge,o}$ from $\mathbf{d}_j$ with calculated $\mathbf{U}_A^c$, $\mathbf{U}_{\text{OI}}^{d,c}$, and $\mathbf{U}_{\text{OI}}^{ge,c}$ with the misfit functions

$$\mathcal{M}_{A_j} = \frac{|\mathbf{U}_A^o - \mathbf{U}_A^c|_j^2}{\sigma_j^{A^2}} \tag{7a}$$

$$\mathcal{M}_{\text{OI}_j}^d = \frac{|\mathbf{U}_{\text{OI}}^{d,o} - \mathbf{U}_{\text{OI}}^{d,c}|_j^2}{\sigma_j^{d^2}} \tag{7b}$$

$$\mathcal{M}_{\text{OI}_j}^{ge} = \frac{|\mathbf{U}_{\text{OI}}^{ge,o} - \mathbf{U}_{\text{OI}}^{ge,c}|_j^2}{\sigma_j^{ge^2}} \tag{7c}$$

$$\mathcal{M} = \frac{1}{3n} \sum_{j=1}^{n} \left(\mathcal{M}_{\text{FB}_j} + \mathcal{M}_{A_j} + \mathcal{M}_{\text{OI}^d_j} + \mathcal{M}_{\text{OI}_j}^{ge} \right) \tag{7d}$$

for a total of n data vectors $\mathbf{d}_j|_{j=1}^{n}$, and the variances σ_j^A, σ_j^d, σ^{ge}. The total misfit, $\mathcal{M}$, was representative of the mean model variance over $\mathbf{d}$ nondimensionalized by the data variances, σ_j^A, σ_j^d, σ_j^g, the vector standard deviations. $\mathcal{M}_{\text{FB}_j}$ was not considered when averaging over the misfit function (hence, $1/3n$ was used rather than $1/4n$), due to its relative magnitude being typically 10% of the misfits in equations (7a) to (7c).

3.4. Inverting Geostrophic Currents Only: Inverse Model $\mathbb{I}_g$

For the case of satellite/reanalysis-derived data with geostrophic currents $\mathbf{U}_{\text{OI}}^{g,o}$ only, the data vector for time point j is

$$\mathbf{d}_j = (\mathbf{U}_{A_x}^o, \mathbf{U}_{A_y}^o, \mathbf{U}_{\text{OI}_x}^{g,o}, \mathbf{U}_{\text{OI}_y}^{g,o})_j. \tag{8}$$

3.4.1. Inverse Model Misfit Functions and Implementation

The force balance misfit $\mathcal{M}_{\text{FB}}$ for this inverse model is as in equation (6) but replacing $\mathbf{U}_{\text{OI}}^{d,o}$ with $\mathbf{U}_{\text{OI}}^{g,o}$

$$\mathcal{M}_{\text{FB}_j} = \frac{1}{\sigma_{\text{FB}}} \left| \left(\frac{m_1}{m_2} \rho_I \exp(im_4) |\mathbf{U}_{A_j}^o| \mathbf{U}_{A_j}^o \right. \right.$$
$$\left. \left. - \frac{\rho_I}{m_2} \exp(i(m_3 + m_4)) |\mathbf{U}_{\text{OI}_j}^{g,o}| \mathbf{U}_{\text{OI}_j}^{g,o} + i\rho_I h_I f_c \mathbf{U}_{\text{OI}_j}^{g,o} \right) \right|^2,$$

Misfit functions were sought for each observed velocity by comparing it with a model calculated quantity. For this inverse model we used the numerical method given in the appendix, equations (A1) to (A3), to predict $\mathbf{U}_{\text{OI}}^{g,c}$ from a given $\mathbf{m}$ and $\mathbf{U}_A^o$, and vice versa. The misfit functions are therefore

$$\mathcal{M}_{A_j} = \frac{|\mathbf{U}_A^o - \mathbf{U}_A^c|_j^2}{\sigma_j^{A^2}} \tag{9a}$$

$$\mathcal{M}_{\text{OI}_j}^g = \frac{|\mathbf{U}_{\text{OI}}^{g,o} - \mathbf{U}_{\text{OI}}^{g,c}|_j^2}{\sigma_j^{g^2}} \tag{9b}$$

$$\mathcal{M} = \frac{1}{2n} \sum_{j=1}^{n} \left(\mathcal{M}_{\text{FB}_j} + \mathcal{M}_{A_j} + \mathcal{M}_{\text{OI}_j}^g \right) \tag{9c}$$

for n data vectors $\mathbf{d}_j$, and data variances, σ_j^A, σ_j^g.

3.5. Numerical Parameter Space Exploration

By seeking the minimal misfit solution, a best fitting model can be found for the given data vectors $\mathbf{d}_j|_{j=1}^{n}$. The parameter search was performed over the domain

$$
\begin{aligned}
0 &\leq Na^2 &&\leq 4 \times 10^{-3} \\
0 &\leq Ro' &&\leq 1.5 \times 10^3 \\
-\pi &< (\theta_{\text{OA}}, \theta_A) &&\leq \pi.
\end{aligned}
$$

chosen to represent all possible physically relevant models, allowing for convergence to optimal models and to reduce the likelihood of convergence to a point upon the domain boundaries for all the inversions

performed in section 4. The range of Na^2 covered the ranges of α^2 (as discussed in section 5.1 and used in equation (A1)) given by Thorndike and Colony (1982; maximum of 0.012^2) and Leppäranta (2005; maximum of 0.035^2). The range of Ro' corresponded to the Rossby number range of $0 < Ro < 2$ as given by Leppäranta (2005).

The cyclic nature of the θ_{OA}, θ_A domains presented the greatest challenge, particularly when trade-offs occur. The development of an inverse model that allows for cyclic parameter domains is a subject for future study.

The parameter search was performed using the Neighborhood Algorithm (Sambridge, 1999b), an efficient Monte Carlo method that enables sampling a multidimensional parameter space. It has repeated sampling loops that perform dense resampling over the neighborhood of the best fitting models. Using this method, one can retrieve optimal solutions to nonlinear inverse problems with relatively few model evaluations compared to full parameter space Monte Carlo sampling. The method has been successfully applied to a wide range of problems in geophysics from earthquake source studies (e.g., Lentas et al., 2014; Sambridge & Kennett, 2001) to estimations of the structure of the Earth's interior (e.g., Berbellini et al., 2017; Snoke & Sambridge, 2002). In addition to the model sampling step, we also performed a Bayesian analysis of the sampled models using the package NA-Bayes (Sambridge, 1999a). This package performs Markov Chain integration of the Monte Carlo simulations to create posterior probability density function (PPDFs) over the retrieved parameter space. As our misfit functions are nondimensionalized by the data variance fitted, the output models obtained from the sampling step could be used directly as the input to the NA-Bayes. The misfit functions (equations (9) and (7)) are coded within the Neighborhood Algorithm forward model routine. The other modifications to the Neighborhood Algorithm include the data input and can be found at https://github.com/hheorton/Freedrift_inverse_submit along with data handling and visualization scripts. The Neighborhood Algorithm was developed and kindly supplied by M. Sambridge (http://www.iearth.org.au/codes/NA/).

3.6. Synthetic Inversion Tests

Here we present controlled inversion tests whereby we test how well our two inversion schemes retrieve a set of arbitrary input parameters: (i) considering surface and geostrophic currents $\mathbb{I}_g^d$ and (ii) considering geostrophic currents only $\mathbb{I}_g$. A series of data vector sets $\mathbf{d}_j$ consistent with the forward model for a chosen input $\mathbf{m}$ were created, such as that shown in Figure 2. First, a range of winds with speed of 1 to 10 m/s and direction varying by 90° were created. For the inversion test considering geostrophic currents only $\mathbb{I}_g$, the chosen wind and $\mathbf{m}$ gives a corresponding $\mathbf{U}_{OI}^g$. For both surface and geostrophic currents $\mathbb{I}_g^d$, a $\mathbf{U}_{OI}^g$ within a range of 0.01 to 0.2 m/s over 90° opposing the winds was also created, allowing for $\mathbf{U}_{OI}^d$ to be calculated using $\mathbf{m}$. Noise was then added to the system: We first added Gaussian noise of an arbitrary spread to $\mathbf{m}$ when creating the synthesized $\mathbf{d}_j$ and then again to each $\mathbf{d}_j$ before the inversion. This method informs us on the quality of the inverse models and on their limitations when considering realistically noisy data.

3.6.1. Synthetic Test Results

The synthetic tests show that the inverse model considering geostrophic currents only ($\mathbb{I}_g$), worked well for synthesized data, retrieving the original input model $\mathbf{m}$ to six significant digits for the case of no noise (synthetic test trade-off available in the supporting information Figure S3). The inverse model considering both surface and geostrophic currents $\mathbb{I}_g^d$ was harder to solve. The misfit $\mathcal{M}_{OI_j}^{ge}$ (equations (7c) and (A7)) for any evaluated θ_{OA} or θ_A differing by more than 1% from the original $\mathbf{m}$, is proportional, to leading order, to $1/Ro'$. This caused the Neighborhood Algorithm to find minimal misfits on the upper bound of Ro', and no meaningful solution could be found. For this reason we removed the geostrophic current misfit $\mathcal{M}_{OI_j}^{ge}$ from our inverse model, allowing for parameters to be retrieved but not including a direct comparison with the available $\mathbf{U}_{OI}^{ge}$ data. Development of the $\mathcal{M}_{OI_j}^{ge}$ misfit function to allow for increased data comparison will improve the inversion and is a topic for further study.

After performing multiple synthetic tests (Figure S3 for example), we expected to retrieve model parameters within 10% of the input parameters used when adding 10% noise to the input data and when considering 10 separate momentum balances for both inverse models $\mathbb{I}_g^d$ and $\mathbb{I}_g$. The distribution of the retrieved parameters was different for each parameter. Both angles θ_{OA} and θ_A had an even and possibly Gaussian spread with a linear trade-off between the two. The Na^2 and Ro' had an uneven distribution with the 25th percentile within 1% of the median and the 75th over 10% of the median (see Figure S3). This distribution is similar to that seen in the real data inversions as presented below in section 4. For the 10% noise case, and for the real data inversions, the data misfit functions $\mathcal{M}_A$ and all $\mathcal{M}_{OI}$ (equations (7a), (7c), (9a), and (9b)) had

a magnitude comparable with the minimum misfit $o(10^{-1})$, with the majority of the scattered best fitting models in Figure 2 having under 10% error compared to the observation vector (grayscale and blue clusters for $\mathbf{U}_A$ and $\mathbf{U}_{OI}^d$, respectively). These clusters are created by calculating each $\mathbf{U}_A^c$, $\mathbf{U}_{OI}^c$ for all evaluated models with total misfit magnitude within 25% of the minimal misfit. The misfit functions can be conceptualized as the nondimensional distance from each scatter point to the tip of the observation vector. The force balance misfit function $\mathcal{M}_{FB}$ was of order 10^{-2} for these models. Experiments where $\mathcal{M}_{FB}$ was artificially raised by a factor 10 to match the data misfits gave improved fit to the geostrophic current vectors but increased the likelihood of trade-offs between θ_{OA} and θ_A.

4. Results

We present results for both data sources in section 2 and their corresponding inverse models: $\mathbb{I}_g^d$ in section 4.1; $\mathbb{I}_g$ in section 4.2. Case studies for a particular time point are shown. We first show the data for each case study together with the predicted observations for the best fitting model obtained from the inversion scheme. We then show the numerical convergence for these case studies illustrating arising parameter space dependencies. This is followed by the complete times series of each data source. Finally, we show the results of the inverse model $\mathbb{I}_g$ for geostrophic currents applied to entire Arctic Ocean. For comparison we also used the inverse model for geostrophic currents only ($\mathbb{I}_g$) to retrieve parameters from the data presented in section 2.1 by omitting the surface currents. These results are included in Table 3.

4.1. Model $\mathbb{I}_g^d$ Applied to Buoy Surface and Geostrophic Currents

4.1.1. Buoy Array 2, 11–20 July 2014

Here we present a case study in which we describe the full data handling and model parameter retrieval. We chose to invert the available data over a 10-day window with Figure 3 showing the daily Buoy 2 data from 11–20 July 2014. From these 10 days of data we filtered out the following cases: days with fewer than four records for any of the vector data, days with average wind speed less than 0.1 m/s, and days with ice concentration less than 10% or where the standard deviation of the any element of the data vector $\mathbf{d}_j$ was greater than its mean. This last criterion on the data variance made the greatest difference to the inversion results. When reducing the standard deviation limit to be at most half of the mean of the data vector, the model parameters were retrieved with greater resolution. However, in that case less than 50% of the data could be used in the inversions and we were left with few cases where more than five data days were available within a 10-day data window. If there are fewer than 5 days of data available, there is insufficient information from the data and the forward model to resolve the model parameters, as the problem becomes nearly underconstrained. The method of filtering used and the normalization of the misfit functions in equations (9) and (7) implies that a day with more persistent wind, drift, and current better describes the free-drifting sea ice forward model. Use of alternative filtering and normalization to emphasize variable rather than persistent winds is a subject for further research.

For the time period shown in Figure 3 9 days passed the filtering. The corresponding mean wind and relative currents were used as input data to the Neighborhood Algorithm along with the variance noted below each plot. The Neighborhood Algorithm then performed a parameter search as shown in Figure 4 with the best fitting model being $\mathbf{m} = (1.40 \times 10^{-3}, 3.61 \times 10^2, 26.2°, -92.3°)$. The NA-Bayes package then performed a Markov Chain sampling of the misfit space producing posterior probability density functions (PPDFs) with median and interquartile range of $\mathbf{m} = (1.44 \pm 0.35 \times 10^{-3}, 3.63 \pm 0.75 \times 10^2, 25.6 \pm 11.0°, -118.6 \pm 15.7°)$. These parameters correspond to drag coefficients of $(C_A, C_O) = (2.85 \times 10^{-3}, 2.42 \times 10^{-3})$. The trade-off plots show that the Neighborhood Algorithm found a single optimal solution to the inverse problem with only a trade-off between the two angles θ_{OA} and θ_A. The optimal solutions present a physically relevant solution for the drag coefficients, with values of the same order of magnitude as the AIDJEX values widely used in the current literature (Coon, 1980; McPhee, 1976).

There is a well-resolved PPDF for both retrieved angles (see PPDFs in the bottom row in Figure 4). The value of θ_{OA} corresponds well to $\theta_O \approx 25°$ and $\theta_A = 0°$ given by CTLT for the same data, but our value of θ_A does not match that of CTLT. This can be clearly seen in Figure 3 where the calculated air stress vector τ_A (wide black arrow) is rotated beyond 90° to the right of the wind vectors, which corresponds to a nonphysical solution. Using an alternative model with $\theta_A = 0°, \theta_O = \theta_{OA}$ gives a physically meaningful force balance and makes a very small change to the magnitude of the misfit functions (equations (6) and (7)), suggesting that the value of θ_A is poorly constrained in this inversion. However, repeating the inversion
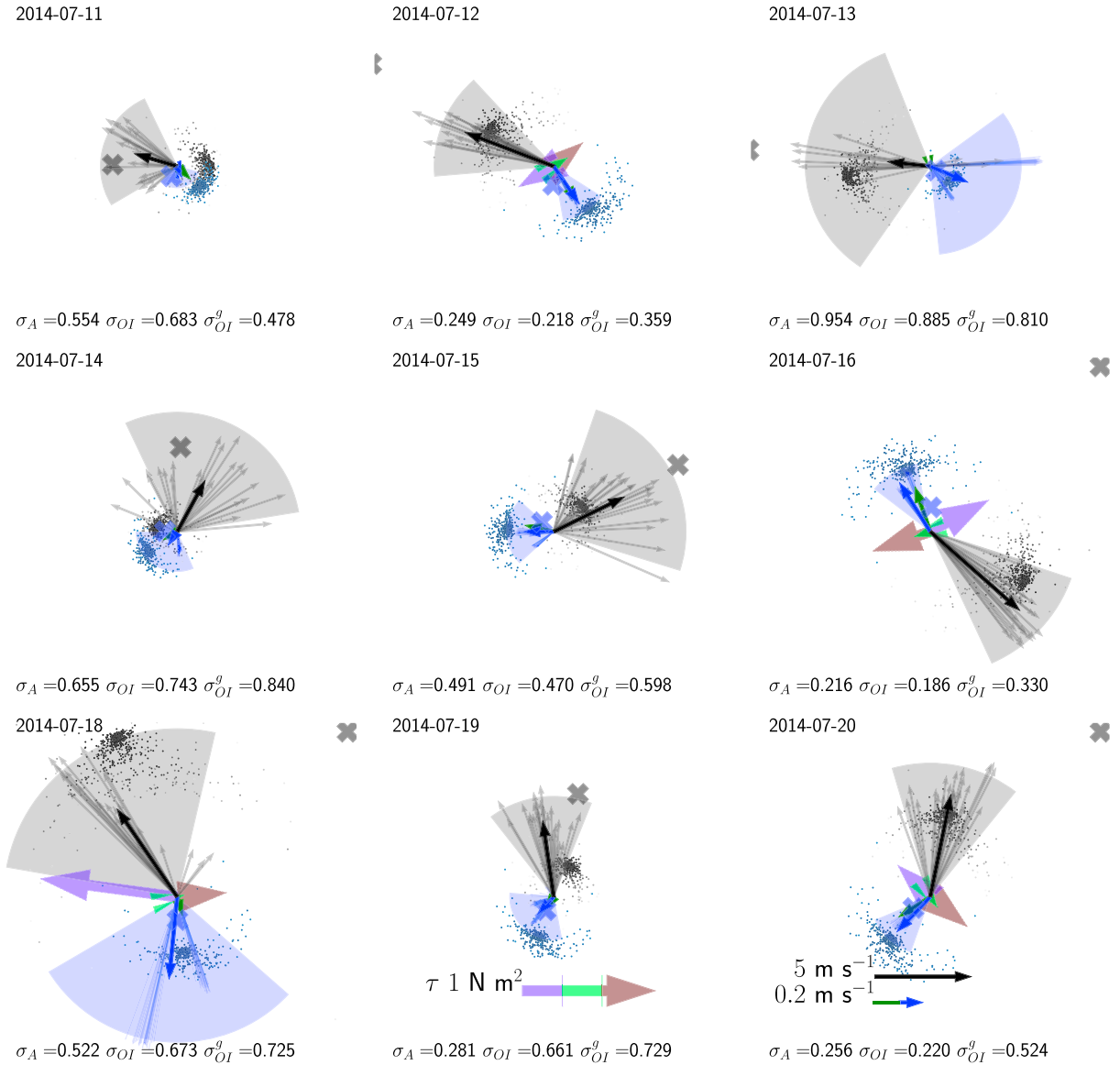
Figure 3. Input data and comparison with the predictions from the best fitting model obtained from the inversion illustrated in Figure 4. We used daily averaged data from Buoy Array 2 obtained between 11 and 20 July 2014. Each subplot corresponds to a day that passed the data filtering. The data were inverted using the inverse model $\mathbb{I}_g^d$. The individual measurements (translucent arrows) and mean (bold arrows) for the wind $\mathbf{U}_A$ (black), relative surface current $\mathbf{U}_{OI}^d$ (blue) and relative geostrophic current $\mathbf{U}_{OI}^g$ (green, small and not visible in several plots) are plotted. The shaded fans represent the data variance. The retrieved model vectors for the best fitting models in Figure 4 are scattered as dots, with lower opacity for greater model misfit (i.e., a poorer data fit) and the AIDJEX model is represented by a cross in the same color as each observation (when the AIDJEX cross lies outside the figure it is listed in its top right corner). The forces given by the observations and the best fitting model are represented by the thick shaded arrows with colors corresponding to Figure 2. The normalized variance for each data subset is listed below each plot.

with a single angle parameter of θ_O and forcing $\theta_A = 0°$ leads to poorer model parameter resolution, with twice as many unusable inversions compared to those in Figure 5 (we define an unusable inversion as one where a parameter value has converged to a point on the search domain boundary).

4.1.2. June–September Buoy Data: Time Series

Figure 5 presents the inversion results using buoy data recorded from 1 June 2014 to the end of the record (the portion of the record with less than 95% ice concentration). The minimal misfit solution for each daily and 10-day averaged inversion is plotted for each buoy with parameter values and associated drag constant on each line plot and PPDF to the left of the figure. The value of the minimal misfit is plotted. The state of the mixed layer at each buoy is represented by the mixed layer depth as given by CTLT along with the associated buoyancy frequency = $\sqrt{g/\rho_O \, \partial\rho_O/\partial z}$ where $g = 9.82$ m/s^2 is the gravitational acceleration and $\partial\rho_O/\partial z$ is
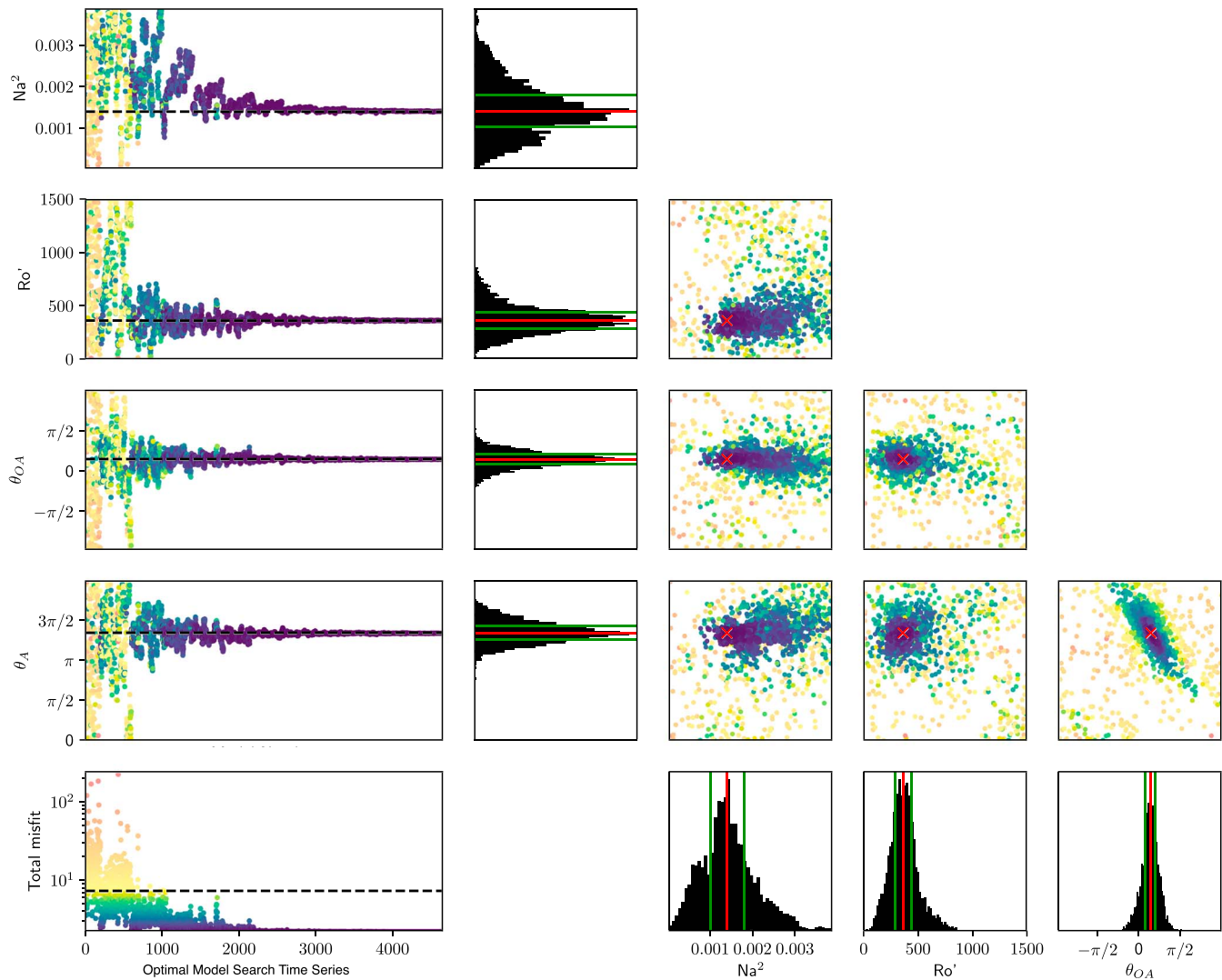
Figure 4. Neighborhood Algorithm convergence, trade-off and Bayesian posterior posterior probability density function s for inverse model $\mathbb{I}_g^d$ applied to daily averaged data from Buoy Array 2 collected in the period 11 and 20 July 2014 (see the data in Figure 3). The plots to the left of the figure display the evolution of the Monte Carlo model evaluations for each parameter aligned with rows of the parameter trade-off matrix on the right. Diagonal features in the latter plots indicate trade-offs between the corresponding parameters displayed in the x and y axes. Each model shown on the rightmost and left plots is colored such that blue points correspond to low misfit values, that is, good data fit, whereas yellow points correspond to high misfit values, that is, poorer data fit. The posterior probability density function for each model parameter is the output of the NA-Bayes Markov chain posterior evaluation with vertical lines representing the median (red) and interquartile range (green).

the rate of change in ocean potential density at the base of the mixed layer. As consecutive inversions will share six to eight data vectors $\mathbf{d}_j$, we expect their solutions to be similar. We therefore reduced the visual impact of any consecutive inversions that differ by any of $\Delta\mathbf{m} > (8 \times 10^{-4}, 500, \pi/2, \pi/2)$. All data are used in the distributions to the left of the figure. As this study is a proof of concept we have chosen to present our inversion results here in full including the poorly constrained results.

The inversion results for all the buoys over the length of the time series plotted are consistent with those shown in Figures 3 and 4. A median model of $\mathbf{m} = (0.75 \times 10^{-3}, 0.22 \times 10^2, 30.4°, \text{NR})$ is obtained, where, due to the amount of unresolved values (values lying upon the domain boundary) of θ_A and values evenly spread over 360°, no meaningful average is obtained. This corresponds to median daily values of $(C_A, C_O) = (2.18 \times 10^{-3}, 4.12 \times 10^{-3})$ increasing to $(C_A, C_O) = (3.14 \times 10^{-3}, 6.54 \times 10^{-3})$ for 10-day averages, with all retrieved drag coefficients displaying a log-normal distribution (C_O histograms in Figure 5 have a close fit to a log-normal distribution). The inversion results for Buoy Arrays 2 and 4 are stable through the time series with an increase in θ_{OA} and smooth changes in C_A and C_O through the daily and 10-day time series. Buoy
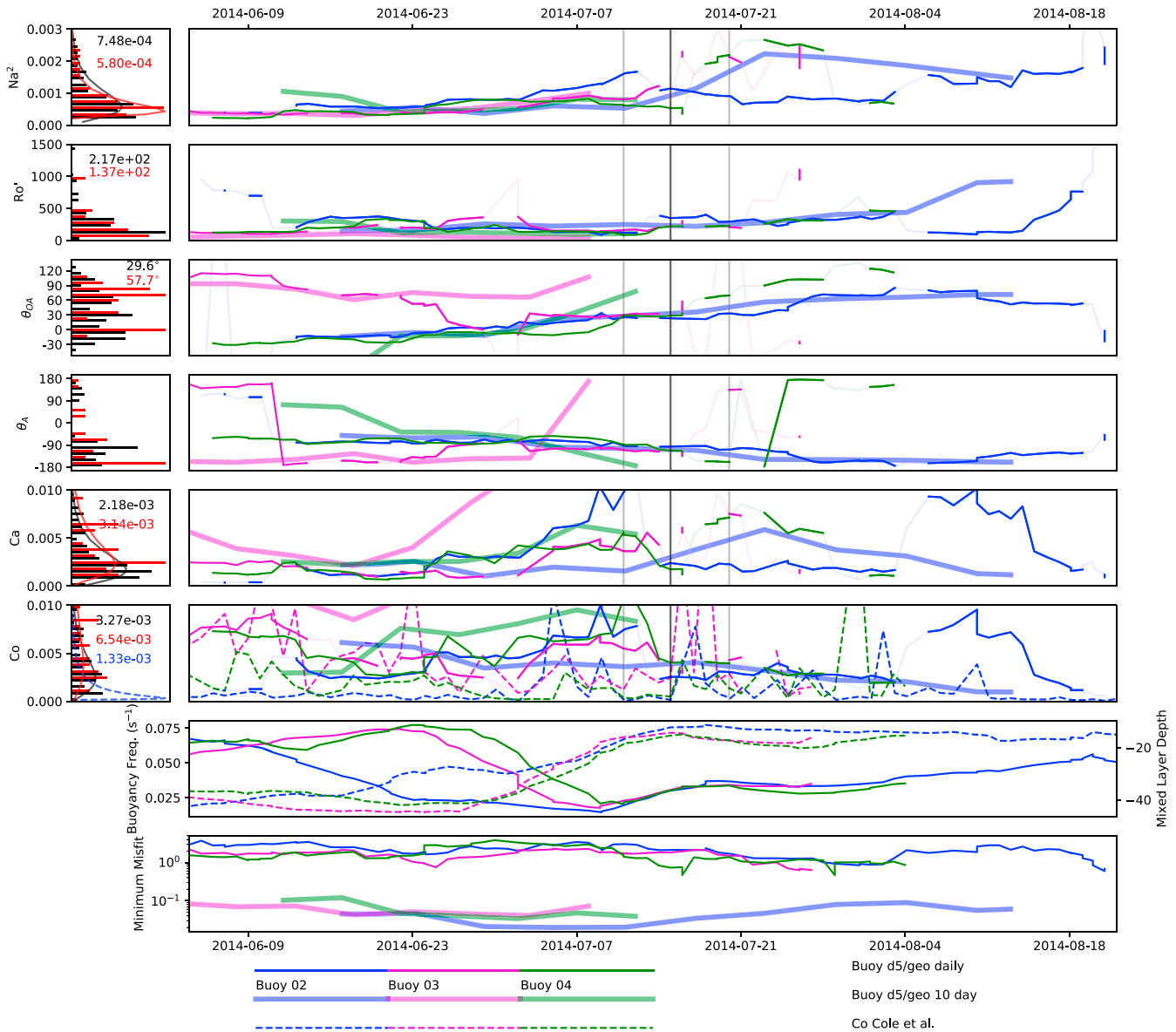
Figure 5. Collected minimum misfit models **m** and C_A, C_O from surface/geostrophic current inversions using buoy data in June–September 2014. Daily averages (thin lines) and 10-day averages (thick lines) are plotted as indicated in the legend. The C_O plot also shows the values calculated by CTLT from surface currents (dashed lines). The histograms on the left show the posterior probability density function of the retrieved parameters from the daily (black) and 10-day (red) averaged data inversions, plus a log-normal fit and median value, where obtainable. The seventh plot shows the mixed layer depth (dashed lines) and the buoyancy frequency (solid lines) from the ITP-V buoy data. The bottom plots shows the value of the minimal misfit. The vertical lines on the top plot show the time period considered in Figures 3 and 4. For daily data we performed 217 separate inversions using $\mathbb{I}_g^d$ and for 10 day data 32 separate inversions. In this plot the well-resolved inversions of daily data are emphasized in order to focus on these results.

Array 3 is more variable, though the higher drag values of CTLT suggest that the ocean currents had higher variability and turbulence than at the other buoy locations. The median value of CTLT's $C_O = 1.3 \times 10^{-3}$ (see blue dashed histogram to the left of the time series) is lower than our results for both the 1- and 10-day averaged data.

Our retrieved C_O values are consistently higher than those given by CTLT. We must accept the validity of the values of C_O given by CTLT for 6-m depth due to the sophisticated means of their retrieval (see section 2.1). This means that the difference from our retrieved C_O to that given by CTLT has a physical reason: the modification of neutral and total drag, the temporal scales the drag coefficients represent, or a bias due to the inversion technique, which is further discussed in section 5. The method used by CTLT to retrieve drag coefficients is representative of hourly flows, while our results are from daily averages. Of particular
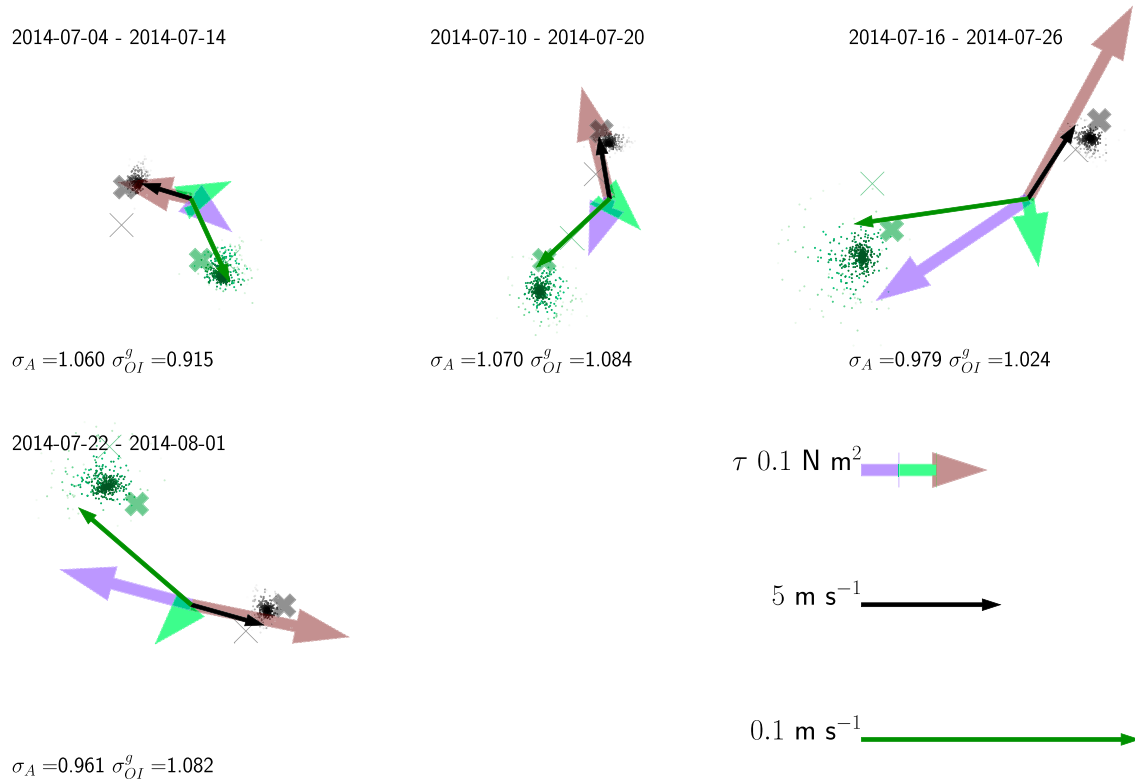
Figure 6. Input data and comparison with the predictions from the best fitting model obtained from the inversion illustrated in Figure 7. We used 10-day averaged satellite data coincident to Buoy Array 2 between 4 July and 7 August 2014. The inverse model used is $\mathbb{I}_g$. The mean wind $\mathbf{U}_A$ (black) and relative geostrophic current $\mathbf{U}_{OI}^g$ (green) are plotted. The retrieved model vectors for the best fitting models in Figure 7 are scattered as dots with lower opacity for greater model misfit (i.e., a poorer data fit), the AIDJEX model is represented by a thick cross and the corresponding buoy array $\mathbb{I}_g$ inversion as a thin cross in the same color as each observation. The forces given by the observations and the best fitting model are represented by the thick shaded arrows with colors corresponding to Figure 2. The normalized variance for each subset of data is listed below each plot.

interest for the comparison with local conditions is a storm and high inertial oscillation observed by CTLT about 22 July. During this period, inversions using data from Buoy Array 3 produced no consistent results (purple lines in Figure 5, which are highly variable and often lie upon domain boundaries) and using the data from Buoy Array 4 leads to an increase in C_A. Melt ponds began draining on 27 June (Gallaher et al., 2016), correlating with the decrease in buoyancy frequency and mixed layer depth obtained from data from Buoy Arrays 3 and 4, while data from Buoy Array 2 show changes from around 10 June. From July onward the buoyancy frequency slowly increased and the mixed layer depth stayed near constant at around 20-m depth. The inverted Na^2 and Ro' (both daily and 10-day averages) are stable for data from all buoys up to mid-July when the ocean mixed layer has shallowed. The derived C_A gives consistent values for Buoy Arrays 2 and 3 for this period, with C_O having higher variability.

4.2. Model $\mathbb{I}_g$ Applied to Satellite and Reanalysis Data Based on 10-Day Averages, Geostrophic Currents Only

4.2.1. Data Coincident to Buoy Array 2, 4 July to 1 August 2014

Here we present an example of the inversion of both satellite and buoy data covering the widest temporal averaging possible. The input data are plotted (Figure 6) along with detailed results from the inversions (Figure 7). These inversions used 10-day averaging periods that overlapped every five days. Five data vectors $\mathbf{d}_j|_{j=1}^5$ were considered for each inversion before the data filtering. The data used in each version therefore covered $\approx$ 30 days. We maximized the averaging period for each individual $\mathbf{d}_j$ while also balancing the total time period covered by all $\mathbf{d}_j|_{j=1}^n$ and the number of data available to the inverse modeling. Due to the variance of winds over 10-day timescales the variance was similar for each data point ≈ 1.0–1.2, and we excluded poor-quality data with standard deviation greater than twice the data's mean.

The inversion results for the satellite data shown in Figure 7 give the best fitting model $\mathbf{m}$ = (0.47 × $10^{-3}, 1.22 \times 10^2, 21.9°, 4.2°$). These parameters correspond to drag coefficients of (C_A, C_O) = (2.84 ×
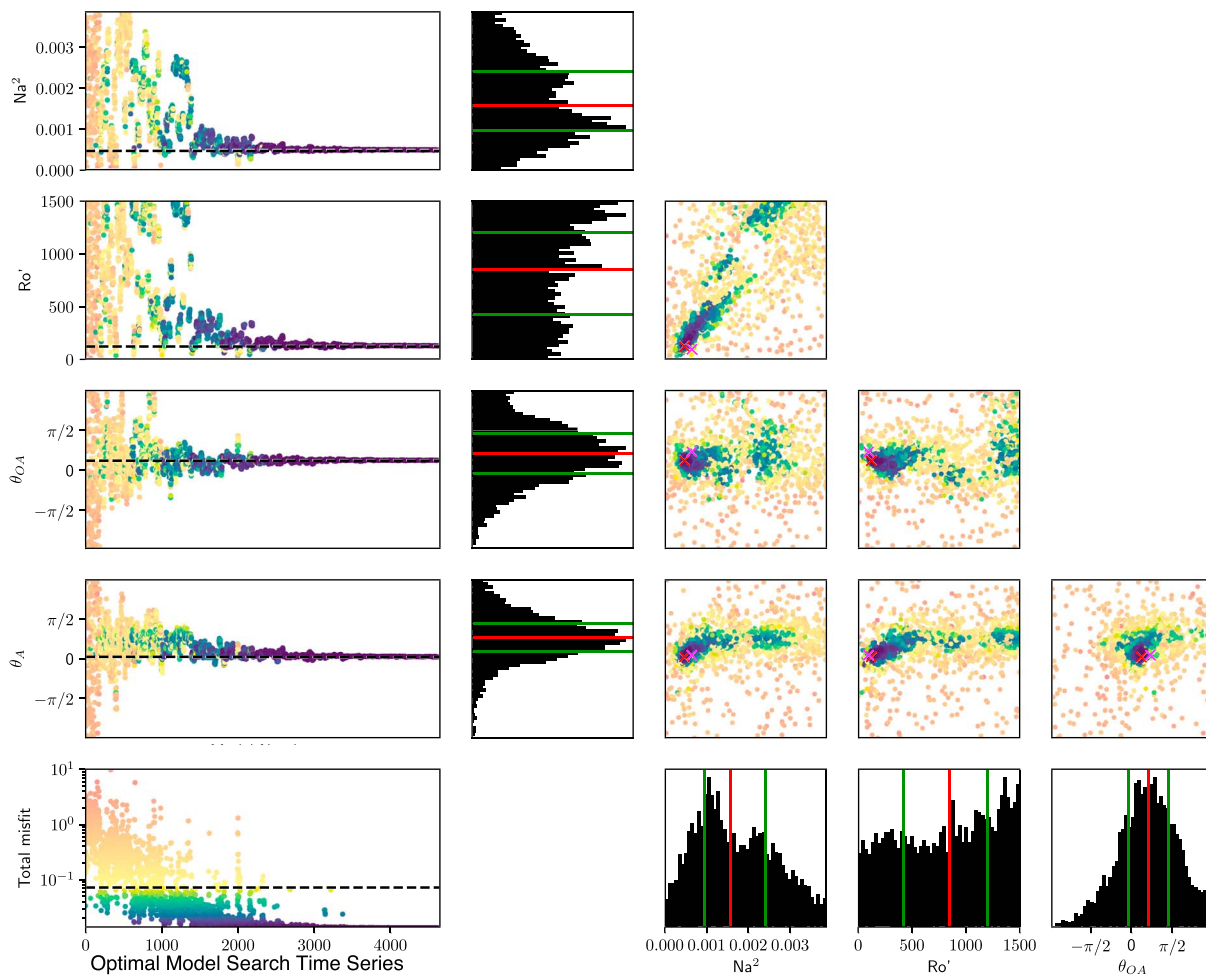
Figure 7. Neighborhood Algorithm convergence, trade-off and Bayesian posterior posterior probability density functions for inverse model $\mathbb{I}_g$ applied to 10-day averaged satellite data coincident to Buoy Array 2 on 4 July to 7 August 2014 (see the data in Figure 6). The plots to the left of the figure display the evolution of the Monte Carlo model evaluations for each parameter aligned with rows of the parameter trade-off matrix on the right. Diagonal features in these plots indicate trade-offs between the corresponding parameters displayed in the x and y axes. Each model shown on the rightmost and left plots is colored such that blue points correspond to low misfit values, that is, good data fit, whereas yellow points correspond to high misfit values, that is, poorer data fit. The red crosses are the minimal misfit model for the satellite data, and the pink crosses for the corresponding buoy array. The posterior probability density function for each model parameter is the output of the NA-Bayes Markov chain posterior evaluation with vertical lines representing the median (red) and interquartile range (green).

10^{-3}, 7.32×10^{-3}). The NA-Bayes package was only able to produce PPDFs for the θ_{OA} and θ_A parameters, showing that there was less information available from the data to resolve parameter values compared to when using the 1-day averaged buoy data in Figure 4. The trade-off plot for the 10-day satellite data (Figure 7) shows a trade-off between the Na^2 and Ro' parameters. However, the retrieved parameters present a model consistent with the AIDJEX standard. The satellite input data (thin black and green lines) in Figure 6 are closely matched by both the predicted observations from our retrieved model (black and green clusters) and the AIDJEX model (black and green crosses), including data covering 22 July 2014 when a storm passed over the buoys location. The resulting force balance for the best model has the wind stress closely aligned to the wind balanced by the ocean stress and Coriolis/tilt forces in accordance with the physical theory.

Comparing with the best fitting model obtained from buoy data for this period (see pink crosses in Figure 7, thin crosses in Figure 6, and 10-day buoy data inversion in supporting information Figure S4), produced a similar best fitting model although with less well resolved parameters than when using satellite data. The 10-day averaged geostrophic current measured by the buoys during this period was more variable in magnitude and direction than those from satellite data.
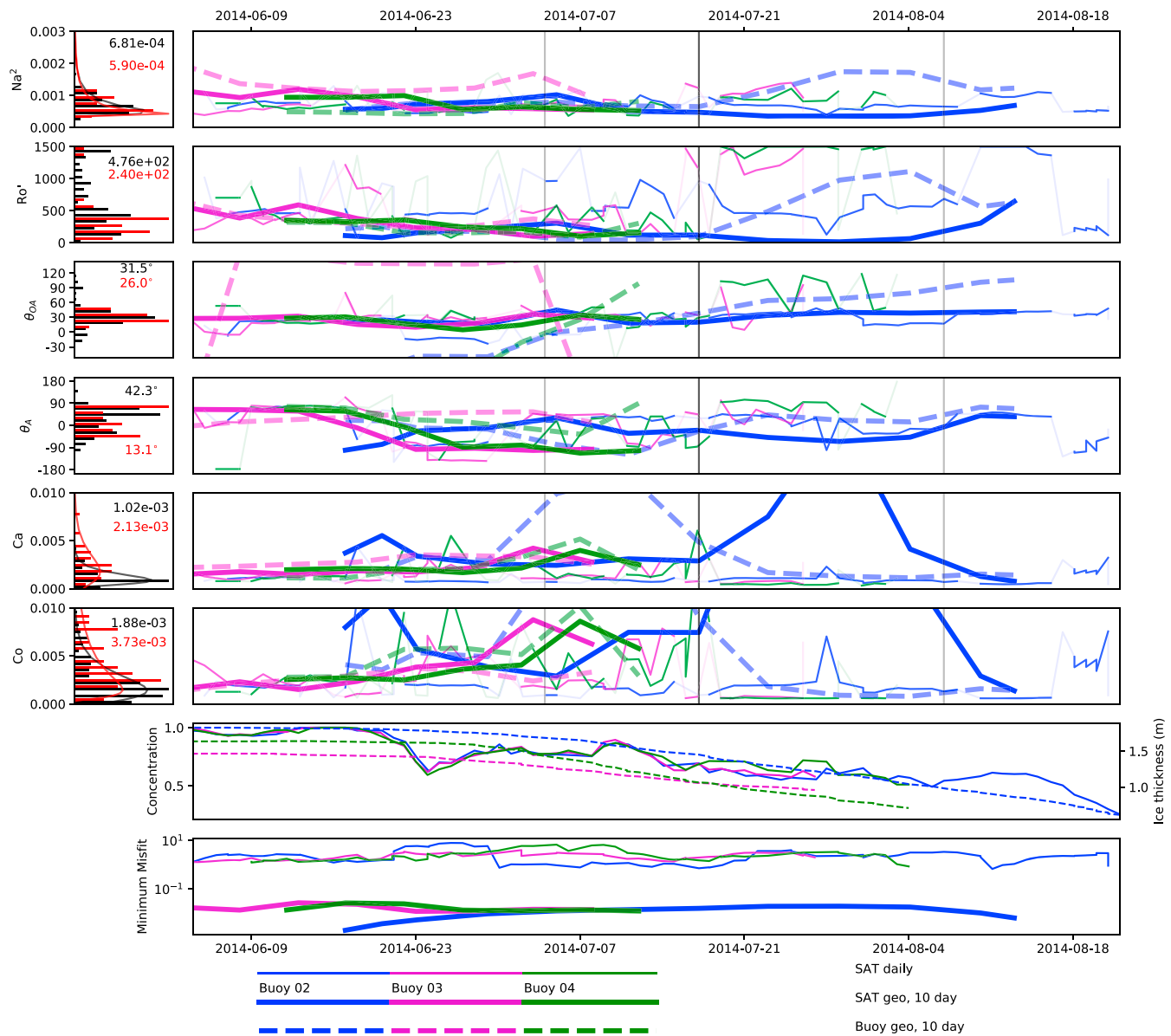
Figure 8. Collected minimum misfit models **m** and C_A, C_O from geostrophic current inversions from using satellite and reanalysis data in June–September 2014. Daily average (thin lines) and 10-day average (thick solid lines) are plotted as indicated in the legend with additional 10-day averaged buoy data inversions (thick dashed lines) for comparison. The histograms on the left show the posterior probability density function of the retrieved parameters from the daily (black) and 10-day (red) data inversions plus a log-normal fit and median value where obtainable. The seventh plots shows the local National Snow and Ice Data Center SSMI sea ice concentration and ice mass balance buoy ice thickness. The bottom plot shows the value of the minimal misfit. The vertical lines on the top plot show the time period considered in Figures 7 and 6.

4.2.2. Full Satellite Inversion Time Series

The inversion results for the satellite and reanalysis data are consistent with the coincident buoy arrays over the time series; see Figure 8. The median 10-day model was $\mathbf{m} = (0.59 \times 10^{-3}, 2.40 \times 10^2, 26.0°, \text{NR})$ with θ_A having a wide unresolved distribution. This corresponds to drag coefficients of $(C_A, C_O) = (2.13 \times 10^{-3}, 3.73 \times 10^{-3})$. A similar result was obtained for the 10-day averaged buoy data (thick dashed lines in Figure 8) for Na^2 and Ro'. The daily data inversions for the satellite and reanalysis data were poorly constrained for the Ro' parameter, although it is possible to gain information about (C_A, C_O) through their distributions. The drag coefficients both increase for a longer time averaging period. When using buoy data from Array 2, the longest time series available, θ_{OA} is seen to increase through the time series as the ice concentration decreases (dashed thick blue line in Figure 8). This development is not seen with the satellite data inversions.
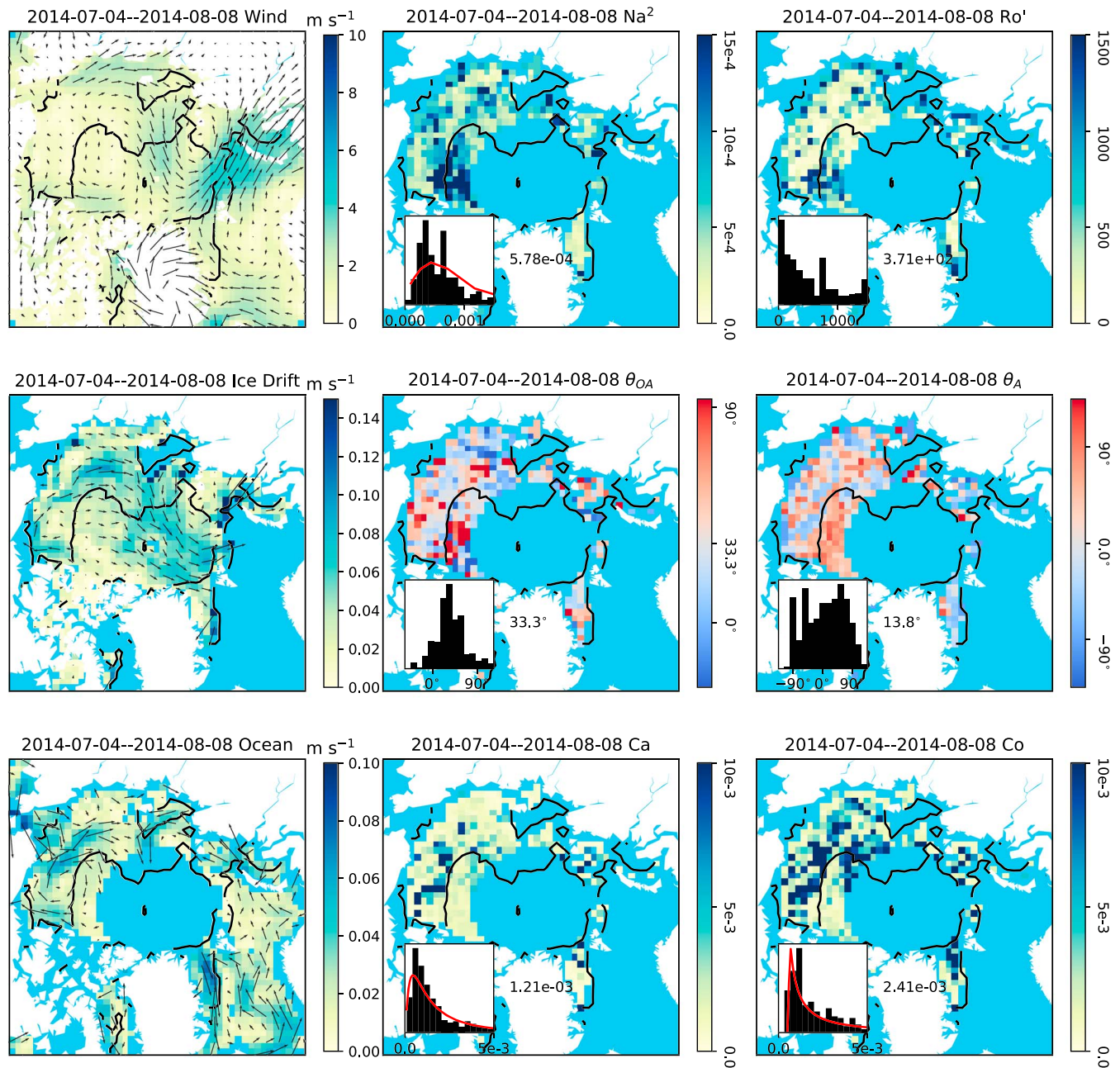
Figure 9. Map of best fitting model parameters **m** from our inversions and resultant (C_A, C_O) from reanalysis data (ERA $\mathbf{U}_A$) and satellite data (Kimura et al., 2013 $\mathbf{U}_I$, CryoSat $\mathbf{U}_O^g$) from separate 10-day averages covering the period 4 July to 8 August 2014. The 15% and 95% contours of National Snow and Ice Data Center SSMI ice concentration are overlaid with posterior probability density functions and with the median of the parameter value within these two contours plotted along with the log-normal fit, where obtainable. The parameters plotted on each individual map pixel result from a separate inversion of data products interpolated onto a grid with 100-km spatial resolution.

As there is a strong correlation between the buoy and satellite winds and ice drift data, it is possible that this difference is due to the different nature of the geostrophic ocean current data or the deviation between buoy and satellite measured ice drift in Figure 1. The local buoy measurements of $\mathbf{U}_O^g$ were subject to shorter time and length scale variations (Cole et al., 2017), whereas the satellite dynamic ocean topography in theory should be immune to short time and length scale flows. We suggest this as the reason for the improved resolution of the satellite 10-day geostrophic only inversions.

Table 1
Summary of Previous Studies of Sea Ice Stress Parameters

Study	$C_{An} \times 10^{-3}$	$C_O \times 10^{-3}$	θ	Notes
McPhee (1976) and Coon (1980)	1.5	5.5	$\theta_O, 24°$	The AIDJEX campaigns
Wamser and Martinson (1993)	1.4–1.9	1.1–1.6	$\theta_O, 18 \pm 18°$	Antarctic, thin or compact ice and MIZ observations
Guest et al. (1995)	1.5–5.6			Summary of MIZ ABL studies
Schröder (2003)	1.9 ± 0.8			MIZ ABL Observations
Shaw et al. (2008)		5.5–10.0	$\theta_O, 27.3°$	From observations of roughness length
Randelhoff et al. (2014)		3.8,3.4	$\theta_O, 39 - 32°$	Two observed events in the Nansen Basin
Cole et al. (2014)		7.1		Beaufort Sea ITP-V turbulence analysis
Cole et al. (2017)		0.4–5.0	$\theta_O^d, 4 - 11° \theta_O^g, 18 - 35°$	Space and time dependent C_O
	Parameterizations			
Lu et al. (2011)		0.5–20.0		Review of observations, new C_O parameterization
Lüpkes et al. (2012)	1.0–2.5			Parameterization for variable drag within a climate model
Castellani et al. (2014)	0.9–2.8			Arctic laser altimetry data forced parameterization
Tsamados et al. (2014)	1.0–2.5	4.0–11.0		Climate model implementing Lüpkes et al. (2012)
Petty et al. (2017)	0.5–1.5			Observations of ice state applied to the above

Note. Atmospheric drag coefficients are for the neutral drag C_{An} before stability correction. C_O are ocean drag coefficients and θ are various turning angles. ABL = atmospheric boundary layer; ITP-V = Ice-Tethered Profilers; MIZ = marginal ice zone.

4.3. Arctic-Wide Satellite Data From July 2014

The data handling and inversion method used to obtain the results shown in Figures 6-8 were repeated for all available data over the Arctic Ocean (Figure 9). The ice thickness for this inversion was taken from the PIOMAS data set (Schweiger et al., 2011). During this time period there was a wide region of sea ice with 15–95% concentration that we assumed to be in free drift and thus consistent with our forward model (see contour lines in Figure 9). Within this region the best fitting median model $\mathbf{m} = (0.57 \times 10^{-3}, 3.71 \times 10^2, 33.3°, 13.8°)$ with associated drag coefficients of $(C_A, C_O) = (1.21 \times 10^{-3}, 2.41 \times 10^{-3})$ was retrieved. The variance of both retrieved drag coefficients is higher than the buoy coincident inversions using the same data set (Table 3). Ice conditions can vary across the Arctic but will remain relatively consistent for the buoy coincident case. While the median and variance are consistent with previous studies (Table 1), there are high values of $C_A \approx 10 \times 10^{-3}$ in the Beaufort Sea. The input data in this location have relatively low winds, ice drift, and geostrophic currents, so we attribute this specific value to a poorly constrained inversion.

The map of Na^2 is smooth with little noise between adjacent pixels, although the results obtained for each pixel came from a separate independent inversion, showing their stability and reliability. The maps of Ro' and thus C_A and C_O are more variable. Patterns of increasing (C_A, C_O) are, however, observable from the Bering Strait and North Alaskan Coast toward the North Pole in alignment with increasing ice concentration up to the contour of 95% in the Beaufort Sea. Beyond this contour within high sea ice concentration there is high Na^2 and θ_{OA} and reduced (C_A, C_O), although the validity of the forward model in this region is doubtful. Both the mean wind and ice drift during this time period (far left panes of Figure 9) are on a bearing approximately southwest from Elsemere Island parallel to northern edge of the Archipelago. This motion is likely to induce high shear internal stresses within the sea ice (Tsamados et al., 2013) and thus cause our forward model (equation (2)) to be invalid.

5. Discussion

This study was a proof of concept of using inverse modeling to analyze the complex nonlinear flow interactions of sea ice-covered seas. We have successfully applied inverse methods to the momentum balance of free-drifting sea ice and retrieved information about the parameters of the quadratic atmospheric and oceanic stress laws. A strength of the inverse modeling is that the parameters are retrieved using the same equations in which they will be used in future study. We have shown the potential of the method with implications for air-ice-ocean dynamics and future work using an inverse modeling approach.

5.1. Arising Parameter Space Dependencies

Within the parameter space of **m**, relationships have arisen. McPhee (2012) suggested that the parameter values depend on the state of the ocean mixed layer, with low θ_O to be expected with fast currents within a deep mixed layer. Figure 5 shows a smooth increase in θ_{OA}, our proxy for θ_O, as the mixed layer becomes shallower for two of the buoys. For shallow mixed layers, which predominantly form during summer sea ice melt, the ocean surface becomes increasingly complex and finding applicable parameter values is harder to do, with CTLT pointing out that the thin freshwater melt layers in particular need to be observed and modeled in order to accurately calculate sea ice-ocean stresses. Park and Stewart (2016) presented such a model that they applied to the Arctic Ocean. Their results showed the emergent turning angle θ_O decreasing with increasing wind speed, although due to differences between their model and the momentum balance used here, direct comparisons are difficult.

The retrieval of flow characteristics using the momentum balance in equation (2) has previously been performed using the complex parameter $A = \alpha e^{i\theta}$ (Thorndike & Colony, 1982; Kwok et al., 2013; Simizu et al., 2014) described by Leppäranta (2005) and used here in this study (equation (A3)). Thorndike and Colony (1982) described the relationship between geostrophic winds and sea ice motion using this method to formulate different flow criteria for each dominating force. Kwok et al. (2013) showed Arctic seasonal cycles in the α and θ parameters, which they attributed to the increased internal ice stresses in winter months. Simizu et al. (2014) used α and θ to analyze flow within the MIZ of the Sea of Okhotsk showing the variation of the parameters for changing ice concentrations. While these previous studies can be seen as quasi-inverse modeling attempts, they stopped short of retrieving usable drag coefficients.

Our values for Na^2 given in Table 3 correspond to the Nansen number or wind-driven factor of 2.7% to 3.5% for the daily averaged data. The 10-day averaged data all give a Nansen number in the range of 2.4% to 2.6%. The associated unscaled Rossby numbers Ro are less well constrained by the inverted data and are in the range 0.25 to 0.52. When considering data with a longer temporal averaging period, there is a decrease in both Nansen and Rossby numbers suggesting that sea ice-to-ocean drag plays an increasing role for longer timescale flow patterns. To compare with Thorndike and Colony (1982), Kwok et al. (2013), and Simizu et al. (2014) who found α increasing in the summer or with decreasing ice concentration A_c, Na^2 is our closest proxy that increases with decreasing A_c in Figure 5. Due to the nonlinearity of the forward problem, it is harder to compare θ to our θ_{OA}. Simizu et al. (2014) observed θ decreasing with lower ice concentrations, while, where reliably obtainable, our θ_{OA} displays an increase (Figures 5 and 9). Whereas our θ_{OA} parameter is related to an accurate relative alignment of stress forces, the θ from Simizu et al. (2014) can be influenced by changing wind speeds and drag coefficients (as in equation (A1)). Thorndike and Colony (1982) described different ice drift circulation patterns for changing wind speed; for example, strong Arctic geostrophic winds have ice drift circulation controlled by Na^2 and θ_{OA}. Through our synthetic test investigations we found that high wind speeds result in both of these parameters being well resolved but left Ro' and θ_A difficult to find or not resolvable. This leads us to the conclusion that data sets $\mathbf{d}_j|_{j=1}^n$ with a variety of wind speeds will allow for the full parameter space to be retrieved. However, as displayed in Figure 3, such a variety of wind and thus ice and ocean velocity may not be representable by a quadratic drag law with a constant parameter space. Also, we considered a constant total atmospheric drag coefficient, rather than a stability modified neutral drag coefficient. For the case of 10-day averages, the data have less variation, Na^2 and θ_{OA} are well resolved but Ro' and θ_A are not (see Figure 6).

When using daily buoy data and inverse model $\mathbb{I}_g^d$, the inversions lead to well-resolved parameters and PPDFs. This can be explained by our use of additional data, notably surface currents at 6- to 7-m depth, and the high fidelity of the buoy data of CTLT. However, the results typically have an unexpected value for θ_A. The forces shown on Figure 3 are aligned at $-90°$ counterclockwise to the expected directions, where, for example, wind stresses are expected to be close to the wind direction. As within our inverse modeling scheme we fitted the magnitude and orientation of the data but only the magnitude of the force balance, there is no way to impose the physicality of stress alignment. Nevertheless, with a physically correct forward model we hope an accurate parameter space will arise such as it does with the case of 10-day data averages. Reducing the parameter space with $\theta_A = 0$ gave a comparable result for Na^2 that is controlled by the ratio of wind and current magnitude, but in order to reduce the errors transferred to the force balance misfit, the parameter search finds maximal values for Ro' and thus no useful values for drag coefficients.

The two angles in the parameter space equation (4) can be seen as a relative alignment θ_{OA} and an offset θ_A. The data misfits, represented as the alignment of the observation arrows and model scatters in Figure 3, allowed the inverse model to retrieve Na^2 and Ro' from their relative magnitude, and θ_{OA} from their relative direction. The accurate retrieval of θ_A requires the consideration of a fixed orientation force, the Coriolis/tilt force at right angles to $\mathbf{U}^g_{OI}$, independent of either θ_{OA} or θ_A. Due to the misfit function $\mathcal{M}^{ge}_{OI}$, equations (7c) and (A7), being unusable in our current configuration when also considering surface currents, $\mathbf{U}^{ge}_{OI}$ is only considered within the other misfit functions, particularly $\mathcal{M}_{FB}$. However, even within the force balance (equation (2)), the Coriolis/tilt force is typically small compared to the stress forces for the daily data available, and thus, θ_A is the least resolved of all the model parameters. For this reason we suggest that the best practical interpretation of our results is taking $\theta_A = 0°$ and $\theta_O = \theta_{OA}$.

Higher drag coefficients are expected when representing flow at closer proximity to a boundary: the law of the wall. We developed two inverse models for this study, $\mathbb{I}^d_g$ for surface and geostrophic currents (section 3.3) and $\mathbb{I}_g$ for geostrophic currents only (section 3.4). Contrasting the results from $\mathbb{I}^d_g$ and $\mathbb{I}_g$ when using the same buoy array data (omitting surface currents in the $\mathbb{I}_g$ case), we see increased retrieved C_O when using surface currents on both 1- and 10-day time scales (see Table 3). This can be contrasted to the relationship between roughness length z_0 and drag parameter C_{dn} at distance z from a boundary

$$C_{dn} = \left(\frac{\kappa}{\ln(z/z_0)} \right)^2 \tag{10}$$

(e.g., Guest & Davidson, 1991) where κ is von-Karman's constant. With a sea ice applicable roughness length of order $z_0 = 10^{-3} \rightarrow 10^{-2}$, changing the ocean drag reference depth from $z = 30$ to 6 m in equation (10) predicts an increase of drag by a factor of ≈ 1.7. Similarly, comparing the retrieved C_O when using surface currents for the sea ice-ocean stress (inverse model $\mathbb{I}^d_g$) compared to using geostrophic currents (inverse model $\mathbb{I}_g$) gives the ratios $4.11/2.41 = 1.7$ applied to 1-day averaged buoy array data in Table 3 and close to the $6.53/2.97 = 2.2$ for 10-day averaged buoy array data. For these examples there is, however, also a change in the retrieved C_A, where we would expect this value to be constant for the identical wind data used in these inversions, implying that the forward model is not entirely consistent with the data. While honoring the limitations of considering two conceptually different data sources, we can also contrast C_A retrieved using the inverse model $\mathcal{I}_g$ applied to spatially coincident buoy array (with 2-m winds) and satellite data (with 10-m winds). There is an increase in C_A of $1.82/1.02 = 1.8$ for 1 day and $2.14/2.12 = 1.01$ for 10-day averaged data, while equation (10) predicts an increase by a factor of ≈ 1.5 for a change in reference height of $z = 2$ to 10 m. Both Na^2 and the drag coefficients have an emergent log-normal distribution, which correlates to the distribution of surface features given by Petty et al. (2017).

5.2. Future Developments

Our data selection based on data variance led to a challenging filtering of high and low wind data. Low winds typically result in relatively high variance, and thus, most data considered for the inversions (see the data fit scatter diagrams in Figure 3) correspond to higher wind speed cases as discussed in section 5.1 (Thorndike & Colony, 1982). Different motion regimes can be simulated with a climate model on an idealized domain such as that used by Heorton et al. (2018) where wind and ocean conditions can be imposed. Such a set up can also be used to investigate the effect of variance measures, forcing wind speed, and the link between the parameter values used on climate model hourly time steps and the emergent daily and monthly motion patterns. Our results suggest that longer time scale vector averaged motion is better represented by higher stress parameters and it will be interesting to see if the relationship extends down to time scales of an hour.

Improvements to the representation of the atmospheric and oceanic boundary layers can be made. In this study we did not account for a stability correction of the drag coefficients to allow for inverse model simplicity. We retrieved the total atmospheric drag C_A, while the neutral drag C_{An} and associated stability correction is of greater use in climate modeling (see section 1). While the assumption of constant C_{An} over the data collection period is in line with the rate of change of sea ice roughness properties (Guest & Davidson, 1991), the atmospheric stability may be more variable (Grachev et al., 2007). There are equational forms for the stability modification (Andreas et al., 2010; Lüpkes et al., 2012) that can be incorporated within the inverse modeling framework and further reanalysis data can be obtained to force these equations (such as from the ERA product used for 10-m winds in this study). For the ocean the measured mixed layer depth and buoyancy frequency (Figure 5) can be considered to force the internal wave ocean stress modification of McPhee

Table 2
Key Mathematical Notation Used in This Study

Notation	Description
$\mathbb{I}_g^d$	Inverse model considering both ocean surface and geostrophic current data
$\mathbb{I}_g$	Inverse model considering ocean geostrophic current data only
d_j	Data input vector for the inverse model
$\mathbf{U}$	Velocity vector
$\mathcal{M}$	Misfit function
$\mathbf{g}$	Forward model
τ	Applied ice stress vector
F_{CT}	Combined Coriolis and ocean surface tilt force vector
$\mathbf{m}$	Model evaluated/retrieved by the inverse model consisting of the following four parameters:
$m_1 = Na^2$	Nansen number squared
$m_2 = Ro'$	Nondimensionalized Rossby number
$m_3 = \theta_{OA}$	Difference between ocean (θ_O) and atmosphere turning angles
$m_4 = \theta_A$	Atmosphere turning angle
C_A	Total atmospheric drag coefficient
C_O	Oceanic drag coefficient
	Subscripts
A	Atmosphere
I	Ice
O	Ocean
OI	Relative ice-ocean velocity
g	Geostrophic
ge	Geostrophic equivalent
d	At depth d (m)
o	Observed (a data point)
c	Calculated
j	Data input vector number
	Additional values
ρ	Density
f_c	Coriolis acceleration (s^{-1})
h_I	Ice thickness m

and Kantha (1989). Moreover, the inverse model can be expanded to consider the entire Ekman spiral (as represented by McPhee, 2012; Park & Stewart, 2016) to investigate how it develops during summer melt, as well as the stratification of the mixed layer that is captured by the data of CTLT.

5.3. Implications of Inverse Model Results

The data sets chosen have proportionalities between wind and relative sea ice-to-ocean velocities that allow for reliable retrieval of the parameters $Na^2 = (\rho_A C_A)/(\rho_O C_O)$ and $\theta_{OA} = \theta_O - \theta_A$, with values for (C_A, C_O) deducible; see Table 2. For the case of 10-day averaged currents collected from an approximately month-long period, our retrieved parameters are within a factor of 2 (less than the range of previously published drag coefficients, see Table 2) of the community standard drag coefficients and turning angles widely used for both buoy and combined satellite and reanalysis data (see section 1). Note that here we compare contemporary neutral atmospheric drag coefficients with our retrieved total atmospheric drag. Our results show that the nonlinear inverse modeling methodology can successfully retrieve parameters from observations of fluid flow, allowing for the retrieval of key parameters over the scale of data availability, while previous studies rely on case studies of turbulent flow structure (e.g., Cole et al., 2017; Elvidge et al., 2016). Our framework simultaneously retrieves both atmosphere and ocean drag coefficients, while previous studies (see Table 1) typically focus on one.

Table 3

Summary of Retrieved Model Parameters for Various Inversion Schemes, Data, and Temporal Averaging Methods Used in This Study

Data used	$Na^2 \times 10^{-4}$	$Ro' \times 10^2$	θ_{OA}	θ_A	$C_A \times 10^{-3}$	$C_O \times 10^{-3}$
AIDJEX "standard"	3.32	1.63	23.0°	0.0°	1.50(C_{An})	5.50
Results for $\mathbb{I}_g^d$, buoy data, 2-m winds, 6-m currents						
Buoy ITP-V	7.48	2.17	30.4°	—	2.18	4.11
$\mathbf{U}_{OI}^d$, $\mathbf{U}_{OI}^{ge}$ 1 day					−0.8,+1.7	−1.6, +2.3
Buoy ITP-V	5.80	1.37	57.7°	—	3.14	6.53
$\mathbf{U}_{OI}^d$, $\mathbf{U}_{OI}^{ge}$ 10 day					−1.0,+2.8	−3.3,+5.1
Results for $\mathbb{I}_g$, buoy data 2-m winds, geo. equiv. currents						
Buoy ITP-V $\mathbf{U}_{OI}^{ge}$ 1 day	12.8	3.70	—	—	1.82	2.41
$\mathbf{U}_{OI}^{ge}$ 1 day					−0.5,+1.0	−1.2, +2.0
Buoy ITP-V	12.3	3.02	—	—	2.14	2.97
$\mathbf{U}_{OI}^{ge}$ 10 day					−0.5,+1.1	−1.3, +2.0
Results for $\mathbb{I}_g$, satellite data, ERA 10-m winds						
Sat/ERA $\mathbf{U}_{OI}^g$ 1 day	6.81	4.76	31.5°	—	1.02	2.21
buoy equivalent					−0.3,+0.4	−0.6, +2.3
Sat/ERA $\mathbf{U}_{OI}^g$ 10 day	5.90	2.40	26.0°	13.1°	2.12	3.73
buoy equivalent					−0.7,+1.1	−1.3, +3.7
Sat/ERA $\mathbf{U}_{OI}^g$	5.78	3.71	33.3°	13.8°	1.21	2.41
10-day Arctic wide					−0.6,+2.5	−1.3, +6.8

Note. See paper text for detailed information on result consistency. The ±quartile range is listed below each drag coefficient. The inverted C^A is the total drag coefficient, the AIDJEX "standard" value is a neutral drag coefficient.

Our study has appraised the application of the forward model. For localized and daily time period motion the physical system is oversimplified. The temporal variation in retrieved parameters is less than the variation in input data (comparing Figure 1 to Figure 5), though there are periods when no consistent model can be found (Buoy 3, 10–30 July). This indicates that the forward model can reproduce aspects of the physical system, though improved representation of winds, local sea ice conditions, and ocean currents is needed, as discussed above in section 5.2. Our results suggest that the forward model of steady state free-drifting sea ice (equation (2)) is best applied to wind, sea ice, and ocean motion average over ≈100-km length scales and time scales greater than 10 days.

We have represented the geostrophic currents $\mathbf{U}_{OI}^g$ by the combination of satellite image derived sea ice drift (Kimura et al., 2013) and dynamic ocean topography-derived ocean currents (Armitage et al., 2016, 2017). Alternatively, we have used the direct buoy measurements of currents at the ocean mixed layer base (Cole et al., 2017) to give an equivalent geostrophic current $\mathbf{U}_{OI}^{ge}$. The latter theoretically arises from the balance of the Coriolis acceleration with the pressure gradient forces considered in the processing of the dynamic ocean topography. On daily time scales buoy measured currents are highly variable and are likely to be dominated by local flows and baroclinic components. When taking 10-day averages the buoy data inversions gave parameters that had increased temporal consistency but were still less physically meaningful than satellite/reanalysis data inversions. There was close correlation between the buoy and satellite/reanalysis-derived wind and ice drift velocities. Hence, we interpret that satellite dynamic ocean topography captured the wide temporal and spatial geostrophic motion of the Arctic Ocean, but our analysis of the ITP-V profiles was more localized in space and time.

Our results showed a decrease in both (C_A, C_O) for a shorter time averaging period (Table 2), in this case from 10 days to 1 day, with collection periods of 1 month and 10 days, respectively (see sections 4.1 and 4.2 for averaging and collection periods). This is true for all studies performed, for both buoy and satellite/reanalysis data; see Table 2 and Figures 5 and 8. In the case of C_O applicable to surface currents, we retrieved values of $C_O = 6.54 \times 10^{-3}$ (10-day averaged data), $C_O = 4.11 \times 10^{-3}$ (1-day averaged data), and

CTLT gave a value of $C_O = 1.22 \times 10^{-3}$ applicable to hourly average flow from the same buoy array data set (see Figure 5). We attribute the difference between our and CTLT's values for C_O to the temporal scale of the data considered. There is also an increase in Na^2, the ratio of the two drag coefficients, for a shorter time averaging period. Differences may also arise due to our exclusion from the analysis of low wind speed conditions (less than 0.1 m/s). If one considers that flow fluctuations about the mean reduce the net transfer of momentum represented by drag coefficients, our results show that it is possible that shorter time scale wind velocity fluctuations (over an hour for example) are less likely to be transferred through the ice cover, to the ocean below, than the daily fluctuations to the monthly mean wind field.

Putting aside the issues of generalizing buoy-based point measurements to the entire Arctic region, our study suggests that values of $(C_A, C_O, \theta_O) = (2.18 \times 10^{-3}, 3.27 \times 10^{-3}, 30.4°)$ are the present-day best applicable parameters (for total drag coefficients) for flows averaged over 1 day, winds at 2-m height, ocean currents at 6-m depth, and sea ice with less than 85% concentration during the summer of 2014. However, when considering a physical system that does not have these very exact specifications, values from a study that better matches the wind, sea ice, and ocean characteristics should be used (Table 1). For example, the value given by CTLT of $C_O = 1.22 \times 10^{-3}$ is better suited for representing the MIZ in a climate model with an hourly time step. Our retrieved values of C_A in Figure 9 show spatially varying Arctic-wide values better suited for 10-day averaged winds at 10-m height. Our results also show temporal variations (Figures 5 and 8), although in practice constant values are still required which our median values in Table 3 are best suited. For the rapidly changing sea ice conditions in the Arctic we can expect sea ice drag coefficients to show both seasonal and yearly variability (Martin et al., 2014, 2016), which can now be investigated using the inverse model developed in this study. The complexity of the sea ice drift physical system makes the choice of drag coefficients to a dynamic sea ice cover challenging. This study has made significant progress in informing the scientific community on what values are most applicable for any future study.

Appendix A: Solutions for the Free Drift Momentum Balance

When only considering ocean current data from one level (inverse model $\mathbb{I}_g$), we used the solution given by Leppäranta (2005) to calculate the $\mathbf{U}_{OI}^g$ from $\mathbf{U}_A$ in accordance with equation (3), with

$$\mathbf{U}_{OI}^g = -\alpha e^{-i\theta}\mathbf{U}_A. \tag{A1}$$

Rearranging equation (3) and substituting equations (4) and (A1) gives

$$Na^2 e^{i\theta_{AO}}|\mathbf{U}_A|\mathbf{U}_A = -\alpha^2 e^{i\theta}|\mathbf{U}_A|\mathbf{U}_A + \alpha Ro' h_I f_c i e^{-i(\theta+\theta_O)}\mathbf{U}_A. \tag{A2}$$

Dividing through by $|\mathbf{U}_A|\mathbf{U}_A$ and taking the real and imaginary parts of equation (A2) gives the following equations for α, θ in terms of $\mathbf{m}$ with

$$\alpha^4 + 2\sin\theta_O Ro'\frac{h_I f_c}{|\mathbf{U}_A|}\alpha^3 + Ro'^2\left(\frac{h_I f_c}{|\mathbf{U}_A|}\right)^2\alpha^2 - Na^4 = 0 \tag{A3a}$$

$$\tan[\theta_A - \theta] = \frac{\alpha\sin\theta_W + Ro' h_I f_c}{\alpha\cos\theta_W}. \tag{A3b}$$

Equation (A3a) was solved consistently using a two-point iterative Newton method (Tiruneh et al., 2013) where $f(\alpha) =$ equation (A3a) and using start points, $\alpha_0 = 0.040, \alpha_1 = 0.035$ and the iterative method

$$s = \frac{f(\alpha_k) - f(\alpha_{k-1})}{\alpha_k - \alpha_{k-1}}$$
$$\alpha_{k+1} = \alpha_{k-1} - \frac{\alpha_{k-1} - \alpha_k}{1 - \frac{f(\alpha_k)}{f(\alpha_{k-1})}\frac{s}{f'(\alpha_k)}}. \tag{A4}$$

For the case of finding $\mathbf{U}_A^c$ from $\mathbf{U}_{OI}^{g,o}$, the full solution for $\mathbf{U}_A^c$ was found for each iteration so to accurately update equation (A2).

For the case taking two separate depths for the ocean stress and Coriolis/tilt force (inverse model $\mathbb{I}_g^d$), the vectors within equation (3) are separable and each of them can be found analytically from the parameter space and the other two. For $\mathbf{U}_A^c$

$$|\mathbf{U}_A^c| = \sqrt{|X|}, \text{ and } \arg(\mathbf{U}_A^c) = \arg(X), \text{ where}$$
$$X = -\frac{1}{Na^2}e^{i(\theta_O - \theta_A)}|\mathbf{U}_{OI}^{d,o}|\mathbf{U}_{OI}^{d,o} - \frac{Ro'}{Na^2}ie^{-i\theta_A}\mathbf{U}_{OI}^{g,o} \tag{A5}$$

and likewise for surface or drag-dependent current $\mathbf{U}_{OI}^{d,c}$

$$|\mathbf{U}_{OI}^{d,c}| = \sqrt{|X|}, \text{ and } \arg(\mathbf{U}_{OI}^{d,c}) = \arg(X), \text{where}$$
$$X = -Na^2e^{i(\theta_A - \theta_O)}|\mathbf{U}_A^o|\mathbf{U}_A^o - Ro'ie^{-i\theta_O}\mathbf{U}_{OI}^{g,o} \tag{A6}$$

and finally for geostrophic current $\mathbf{U}_{OI}^{g,c}$

$$\mathbf{U}_{OI}^{g,c} = \frac{Na^2}{Ro'}ie^{i(\theta_A)}|\mathbf{U}_A^o|\mathbf{U}_A^o + \frac{1}{Ro'}ie^{i\theta_O}|\mathbf{U}_{OI}^{d,o}|\mathbf{U}_{OI}^{d,o}. \tag{A7}$$

References

Aagaard, K., & Carmack, E. C. (1989). The role of sea ice and other fresh water in the Arctic circulation. *Journal of Geophysical Research*, *94*(C10), 14485. https://doi.org/10.1029/JC094iC10p14485

Andreas, E. L., Horst, T., Grachev, A. A., Persson, P. O. G., Fairall, C. W., Guest, P. S., & Jordan, R. E. (2010). Parametrizing turbulent exchange over summer sea ice and the marginal ice zone. *Quarterly Journal of the Royal Meteorological Society*, *136*(649), 927–943. https://doi.org/10.1002/qj.618

Armitage, T. W. K., Bacon, S., Ridout, A. L., Petty, A. A., Wolbach, S., & Tsamados, M. (2017). Arctic Ocean surface geostrophic circulation 2003–2014. *The Cryosphere*, *11*(4), 1767–1780.

Armitage, T. W. K., Bacon, S., Ridout, A. L., Thomas, S. F., Aksenov, Y., & Wingham, D. J. (2016). Arctic sea surface height variability and change from satellite radar altimetry and GRACE, 2003–2014. *Journal of Geophysical Research: Oceans*, *121*, 4303–4322. https://doi.org/10.1002/2015JC011579

Berbellini, A., Morelli, A., & Ferreira, A. M. G. (2017). Crustal structure of northern Italy from the ellipticity of Rayleigh waves. *Physics of the Earth and Planetary Interiors*, *265*, 1–14. https://doi.org/10.1016/j.pepi.2016.12.005

Carmack, E., Polyakov, I., Padman, L., Fer, I., Hunke, E., Hutchings, J., & Winsor, P. (2015). Toward quantifying the increasing role of oceanic heat in sea ice loss in the New Arctic. *Bulletin of the American Meteorological Society*, *96*(12), 2079–2105. https://doi.org/10.1175/BAMS-D-13-00177.1

Castellani, G., Lüpkes, C., Hendricks, S., & Gerdes, R. (2014). Variability of Arctic sea-ice topography and its impact on the atmospheric surface drag. *Journal of Geophysical Research: Oceans*, *119*, 6743–6762. https://doi.org/10.1002/2013JC009712

Cavalieri, D. (1996). *Sea ice concentrations from Nimbus-7 SMMR and DMSP SSM/I-SSMIS passive microwave data, version 1*. Boulder, CO: NASA National Snow and Ice Data Center Distributed Active Archive Center. https://doi.org/10.5067/8GQ8LZQVL0VL

Cole, S. T., Timmermans, M. L., Toole, J. M., Krishfield, R. A., & Thwaites, F. T. (2014). Ekman veering, internal waves, and turbulence observed under Arctic sea ice. *Journal of Physical Oceanography*, *44*(5), 1306–1328. https://doi.org/10.1175/JPO-D-12-0191.1

Cole, S. T., Toole, J. M., Lele, R., Timmermans, M. L., Gallaher, S. G., Stanton, T. P., & Haas, C. (2017). Ice and ocean velocity in the Arctic marginal ice zone: Ice roughness and momentum transfer. *Elementa Science of the Anthropocene*, *5*, 27. https://doi.org/10.1525/elementa.241

Coon, M. D. (1980). A review of AIDJEX modeling, *Sea ice processes and models* (pp. 12–27). Seattle: University of Washington Press.

Davis, P. E. D., Lique, C., Johnson, H. L., & Guthrie, J. D. (2016). Competing effects of elevated vertical mixing and increased freshwater input on the stratification and sea ice cover in a changing Arctic Ocean. *Journal of Physical Oceanography*, *46*(5), 1531–1553. https://doi.org/10.1175/JPO-D-15-0174.1

Dee, D. P., Uppala, S. M., Simmons, A. J., Berrisford, P., Poli, P., Kobayashi, S., & Vitart, F. (2011). The ERA-Interim reanalysis: Configuration and performance of the data assimilation system. *Quarterly Journal of the Royal Meteorological Society*, *137*(656), 553–597. https://doi.org/10.1002/qj.828

Dewey, S., Morison, J., Kwok, R., Dickinson, S., Morison, D., & Andersen, R. (2017). Arctic ice-ocean coupling and gyre equilibration observed with remote sensing. *Geophysical Research Letters*, *45*, 1499–1508. https://doi.org/10.1002/2017GL076229

Dotto, T. S., Garabato, A. N., Bacon, S., Tsamados, M., Holland, P. R., Hooley, J., & Meredith, M. P. (2018). Variability of the Ross Gyre, Southern Ocean: Drivers and responses revealed by satellite altimetry. *Geophysical Research Letters*, *45*, 6195–6204. https://doi.org/10.1029/2018GL078607

Ekman, V. W. (1905). On the influence of the Earth's rotation on ocean-currents. *Arkiv för Matematik, Astronomi och Fysik*, *2*, 1–52.

Elvidge, A. D., Renfrew, I. A., Weiss, A. I., Brooks, I. M., Lachlan-Cope, T. A., & King, J. C. (2016). Observations of surface momentum exchange over the marginal ice zone and recommendations for its parametrisation. *Atmospheric Chemistry and Physics*, *16*(3), 1545–1563. https://doi.org/https://doi.org/10.5194/acp-16-1545-2016

Gallaher, S. G., Stanton, T. P., Shaw, W. J., Cole, S. T., Toole, J. M., Wilkinson, J. P., & Hwang, B. (2016). Evolution of a Canada Basin ice-ocean boundary layer and mixed layer across a developing thermodynamically forced marginal ice zone. *Journal of Geophysical Research: Oceans*, *121*, 6223–6250. https://doi.org/10.1002/2016JC011778

Giles, K. A., Laxon, S. W., Ridout, A. L., Wingham, D. J., & Bacon, S. (2012). Western Arctic Ocean freshwater storage increased by wind-driven spin-up of the Beaufort Gyre. *Nature Geoscience*, *5*(3), 194–197. https://doi.org/10.1038/ngeo1379

Grachev, A. A., Andreas, E. L., Fairall, C. W., Guest, P. S., & Persson, P. O. G. (2007). SHEBA flux–profile relationships in the stable atmospheric boundary layer. *Boundary-Layer Meteorology*, *124*(3), 315–333. https://doi.org/10.1007/s10546-007-9177-6

Guest, P. S., & Davidson, K. (1991). The aerodynamic roughness of different types of sea ice. *Journal of Geophysical Research*, *96*(C3), 4709–4721.

Guest, P. S., Glendening, J. W., & Davidson, K. L. (1995). An observational and numerical study of wind stress variations within marginal ice zones. *Journal of Geophysical Research*, *100*(C6), 10,887–10,904.

Haine, T. W. N., Curry, B., Gerdes, R., Hansen, E., Karcher, M., Lee, C., & Woodgate, R. (2015). Arctic freshwater export: Status, mechanisms, and prospects. *Global and Planetary Change*, *125*, 13–35. https://doi.org/10.1016/j.gloplacha.2014.11.013

Heorton, H. D. B. S., Feltham, D. L., & Hunt, J. C. R. (2014). The Response of the Sea Ice Edge to Atmospheric and Oceanic Jet Formation. *Journal of Physical Oceanography*, *44*(9), 2292–2316. https://doi.org/10.1175/JPO-D-13-0184.1

Heorton, H. D. B. S., Feltham, D. L., & Tsamados, M. (2018). Stress and deformation characteristics of sea ice in a high-resolution, anisotropic sea ice model. *Philosophical Transactions of the Royal Society A*, *376*(2129), 20170349. https://doi.org/10.1098/rsta.2017.0349

Hibler, W. D. (1979). A dynamic thermodynamic sea ice model. *Journal of Physical Oceanography*, *9*(4), 815–846. https://doi.org/10.1175/1520-0485(1979)009<0815:ADTSIM>2.0.CO;2

Holland, M. M., Bitz, C. M., Hunke, E. C., Lipscomb, W. H., & Schramm, J. L. (2006). Influence of the sea ice thickness distribution on polar climate in CCSM3. *Journal of Climate*, *19*(11), 2398–2414.

Kimura, N., Nishimura, A., Tanaka, Y., & Yamaguchi, H. (2013). Influence of winter sea-ice motion on summer ice cover in the Arctic. *Polar Research*, *32*(1), 20193. https://doi.org/10.3402/polar.v32i0.20193

Kwok, R., Spreen, G., & Pang, S. (2013). Arctic sea ice circulation and drift speed: Decadal trends and ocean currents. *Journal of Geophysical Research: Oceans*, *118*, 2408–2425. https://doi.org/10.1002/jgrc.20191

Lentas, K., Ferreira, A. M. G., Clévédé, E., & Roch, J. (2014). Source models of great earthquakes from ultra low-frequency normal mode data. *Physics of the Earth and Planetary Interiors*, *233*, 41–67. https://doi.org/10.1016/j.pepi.2014.05.011

Leppäranta, M. (2005). *The drift of sea ice*. Berlin; New York: Chichester, UK: Springer; Praxis. OCLC: ocm54777756.

Lu, P., Li, Z., Cheng, B., & Leppäranta, M. (2011). A parameterization of the ice-ocean drag coefficient. *Journal of Geophysical Research*, *116*, C07019. https://doi.org/10.1029/2010JC006878

Lüpkes, C., & Gryanik, V. M. (2015). A stability-dependent parametrization of transfer coefficients for momentum and heat over polar sea ice to be used in climate models. *Journal of Geophysical Research: Atmospheres*, *120*, 552–581. https://doi.org/10.1002/2014JD022418

Lüpkes, C., Gryanik, V. M., Hartmann, J., & Andreas, E. L. (2012). A parametrization, based on sea ice morphology, of the neutral atmospheric drag coefficients for weather prediction and climate models. *Journal of Geophysical Research*, *117*, D13112. https://doi.org/10.1029/2012JD017630

Martin, T., Steele, M., & Zhang, J. (2014). Seasonality and long-term trend of Arctic Ocean surface stress in a model. *Journal of Geophysical Research: Oceans*, *119*, 1723–1738. https://doi.org/10.1002/2013JC009425

Martin, T., Tsamados, M., Schroeder, D., & Feltham, D. L. (2016). The impact of variable sea ice roughness on changes in Arctic Ocean surface stress: A model study. *Journal of Geophysical Research: Oceans*, *121*, 1931–1952. https://doi.org/10.1002/2015JC011186

McPhee, M. G. (1976). Ice-ocean momentum transfer for the AIDJEX ice model. *AIDJEX Bulletin*, *29*, 93–111.

McPhee, M. G. (2012). Advances in understanding ice–ocean stress during and since AIDJEX. *Cold Regions Science and Technology*, *76*, 24–36. https://doi.org/10.1016/j.coldregions.2011.05.001

McPhee, M. G., & Kantha, L. H. (1989). Generation of internal waves by sea ice. *Journal of Geophysical Research*, *94*(C3), 3287–3302. https://doi.org/10.1029/JC094iC03p03287

Meneghello, G., Marshall, J., Timmermans, M. L., & Scott, J. (2018). Observations of seasonal upwelling and downwelling in the Beaufort Sea mediated by sea ice. *Journal of Physical Oceanography*, *48*(4), 795–805. https://doi.org/10.1175/JPO-D-17-0188.1

Monin, A. S., & Obukhov, A. M. (1954). Basic laws of turbulent mixing in the surface layer of the atmosphere. *Contributions of the Geophysical Institute of the Slovak Academy of Sciences*, *24*(151), 163–187.

Overland, J. E., & Davidson, K. L. (1992). Geostrophic drag coefficients over sea ice. *Tellus A: Dynamic Meteorology and Oceanography*, *44*, 54–66.

Park, H. S., & Stewart, A. L. (2016). An analytical model for wind-driven Arctic summer sea ice drift. *The Cryosphere*, *10*(1), 227–244. https://doi.org/10.5194/tc-10-227-2016

Petrie, R. E., Shaffrey, L. C., & Sutton, R. T. (2015). Atmospheric impact of Arctic sea ice loss in a coupled ocean–Atmosphere Simulation. *Journal of Climate*, *28*(24), 9606–9622.

Petty, A. A., Tsamados, M. C., & Kurtz, N. T. (2017). Atmospheric form drag coefficients over Arctic sea ice using remotely sensed ice topography data, spring 2009–2015. *Journal of Geophysical Research: Earth Surface*, *122*, 1472–1490. https://doi.org/10.1002/2017JF004209

Randelhoff, A., Sundfjord, A., & Renner, A. H. H. (2014). Effects of a shallow pycnocline and surface meltwater on sea ice–ocean drag and turbulent heat flux. *Journal of Physical Oceanography*, *44*(8), 2176–2190. https://doi.org/10.1175/JPO-D-13-0231.1

Renfrew, I. A., Elvidge, A. D., & Edwards, J. M. (2019). Atmospheric sensitivity to marginal-ice-zone drag: Local and global responses. *Quarterly Journal of the Royal Meteorological Society*, *145*, 1165–1179. https://doi.org/10.1002/qj.3486

Rio, M. H., & Hernandez, F. (2003). High-frequency response of wind-driven currents measured by drifting buoys and altimetry over the world ocean. *Journal of Geophysical Research*, *108*(C8), 3283. https://doi.org/10.1029/2002JC001655

Rippeth, T. P., Lincoln, B. J., Lenn, Y. D., Green, J. A. M., Sundfjord, A., & Bacon, S. (2015). Tide-mediated warming of Arctic halocline by Atlantic heat fluxes over rough topography. *Nature Geoscience*, *8*(3), 191–194. https://doi.org/10.1038/ngeo2350

Rudels, B. (2011). Arctic Ocean circulation and variability-advection and external forcing encounter constraints and local processes. *Ocean Science Discussions*, *8*, 6.

Sambridge, M. (1999a). Geophysical inversion with a neighbourhood algorithm—II. Appraising the ensemble. *Geophysical Journal International*, *138*(3), 727–746. https://doi.org/10.1046/j.1365-246x.1999.00900.x

Sambridge, M. (1999b). Geophysical inversion with a neighbourhood algorithm—I. Searching a parameter space. *Geophysical Journal International*, *138*(2), 479–494. https://doi.org/10.1046/j.1365-246X.1999.00876.x

Sambridge, M., & Kennett, B. (2001). Seismic event location: Nonlinear inversion using a neighbourhood algorithm. *Pure and Applied Geophysics*, *158*(1), 241–257. https://doi.org/10.1007/PL00001158

Schröder, D. (2003). On the parameterization of turbulent surface fluxes over heterogeneous sea ice surfaces. *Journal of Geophysical Research*, *108*(C6), 3195. https://doi.org/10.1029/2002JC001385

Schweiger, A., Lindsay, R., Zhang, J., Steele, M., Stern, H., & Kwok, R. (2011). Uncertainty in modeled Arctic sea ice volume. *Journal of Geophysical Research*, *116*, C00D06. https://doi.org/10.1029/2011JC007084

Shaw, W. J., Stanton, T. P., McPhee, M. G., & Kikuchi, T. (2008). Estimates of surface roughness length in heterogeneous under-ice boundary layers. *Journal of Geophysical Research*, *113*, C08030. https://doi.org/10.1029/2007JC004550

Simizu, D., Ohshima, K. I., Ono, J., Fukamachi, Y., & Mizuta, G. (2014). What drives the southward drift of sea ice in the Sea of Okhotsk? *Progress in Oceanography*, *126*, 33–43. https://doi.org/10.1016/j.pocean.2014.05.013

Snoke, J. A., & Sambridge, M. (2002). Constraints on the *S* wave velocity structure in a continental shield from surface wave data: Comparing linearized least squares inversion and the direct search neighbourhood algorithm. *Journal of Geophysical Research*, *107*(B5), 2094. https://doi.org/10.1029/2001JB000498

Thorndike, A. S., & Colony, R. (1982). Sea ice motion in response to geostrophic winds. *Journal of Geophysical Research*, *87*, 5845. https://doi.org/10.1029/JC087iC08p05845

Tiruneh, A. T., Ndlela, W. N., & Nkambule, S. J. (2013). A two-point Newton method suitable for nonconvergent cases and with super-quadratic convergence. *Advances in Numerical Analysis*, *2013*, 1–7. https://doi.org/10.1155/2013/687382

Tsamados, M., Feltham, D. L., Schroeder, D., Flocco, D., Farrell, S. L., Kurtz, N., & Bacon, S. (2014). Impact of variable atmospheric and oceanic form drag on simulations of Arctic sea ice. *Journal of Physical Oceanography*, *44*(5), 1329–1353. https://doi.org/10.1175/JPO-D-13-0215.1

Tsamados, M., Feltham, D. L., & Wilchinsky, A. V. (2013). Impact of a new anisotropic rheology on simulations of Arctic sea ice. *Journal of Geophysical Research: Oceans*, *118*, 91–107. https://doi.org/10.1029/2012JC007990

Wamser, C., & Martinson, D. G. (1993). Drag coefficients for winter Antarctic pack ice. *Journal of Geophysical Research*, *98*(C7), 12431. https://doi.org/10.1029/93JC00655

Yang, J. (2009). Seasonal and interannual variability of downwelling in the Beaufort Sea. *Journal of Geophysical Research*, *114*, C00A14. https://doi.org/10.1029/2008JC005084

Zhong, W., Steele, M., Zhang, J., & Zhao, J. (2017). Greater role of geostrophic currents in Ekman dynamics in the western Arctic Ocean as a mechanism for Beaufort Gyre stabilization. *Journal of Geophysical Research: Oceans*, *123*, 149–165. https://doi.org/10.1002/2017JC013282